Controllable spin-dynamic scenarios on zigzag carbon cross structure

Jing Liu [1,*] Yiming Zhang,[2] Chun Li [2,†] Wei Jin,[3] Georgios Lefkidis [1,2,‡] and Wolfgang Hübner[1]
[1]*Department of Physics, University of Kaiserslautern, P.O. Box 3049, 67653 Kaiserslautern, Germany*
[2]*School of Mechanics, Civil Engineering and Architecture, Northwestern Polytechnical University, Xi'an 710072, China*
[3]*School of Physics and Information Technology, Shaanxi Normal University, Xi'an 710119, China*

(Received 13 April 2022; revised 3 August 2022; accepted 5 August 2022; published 1 September 2022)

We investigate the spin-dynamic properties of two carbon cross structures assembled from two carbon chains with two Ni atoms attached. Both the global spin transfer through the long-distance carbon cross and the local spin flip on the single Ni atom are achieved within the subpicosecond regime, demonstrating the feasibility of individual intrasite and intersite spin manipulation. We investigate the dependence of the two different types of spin-dynamics processes on an external magnetic field, and we compare them by analyzing the spin features of the populated intermediate states. The comparison explains well the addressability of the local spin flip and the conservation of the global spin transfer. In addition, by applying two identical laser pulses, we successfully enhance the sensitivity of the local spin flip with respect to the external magnetic field, which yields a higher spatial resolution of the individual spin addressing. The present investigation is a significant step towards integrated all-optical logic circuits based on nano-spintronics.

DOI: 10.1103/PhysRevB.106.094401

I. INTRODUCTION

In today's heavily computerized world, the need to miniaturize logic processing units is becoming increasingly important [1–13]. Based on well-developed top-down technology, the size of complementary metal-oxide semiconductors (CMOS) has decreased from 32 to 5 nm during the past 10 years, which is a great achievement for CMOS technology [14–16]. However the rapid miniaturization also indicates that traditional logic devices come closer to their physical limits. Therefore, finding new alternatives is more urgent now. One of the promising solutions is utilizing nano-spintronics [17–20]. The idea is that one can design various logic operations based on the different ultrafast spin-dynamics scenarios of magnetic molecules or clusters. The discrete levels and the highly localized spin density of these molecular systems are instrumental in achieving controllable spin dynamics on a microscopic scale [21–25]. To generate a complete integrated spin logic processor, it is necessary to find proper magnetic molecules or clusters and integrate them into heterostructures.

Since Beaurepaire *et al.* reported the ultrafast laser-induced demagnetization of ferromagnetic Ni [1], there has been a huge amount of progress in both theoretical and experimental investigations of ultrafast spin dynamics [26–33]. In particular, the investigations of single molecular spintronics have uncovered many intriguing spin-dynamic properties, ensuring their great potential for application in the basic elements of future integrated logic processors [34–38]. For examples, Mahan suggested a one-dimensional shift register consisting of N identical atoms [39]. Luis *et al.* proposed spin-based CNOT and SWAP quantum gates by using two weakly coupled Tb^{3+} as spin qubits [40]. Jenkins *et al.* mapped eight well-defined spin states of GdW_{30} to the basis states of three qubits [41]. Godfrin *et al.* implemented Grover's quantum algorithm via nuclear spin of a Tb ion in a single molecular magnet transistor [42]. Macalluso *et al.* encoded a qubit with an embedded quantum error correction on a molecular trinuclear coordination compound [43]. Liu *et al.* demonstrated coherent electrical control of the quantum spin state, and they exploited it to independently manipulate the two magnetically identical but inversion-related molecules in the unit cell of a crystal [44]. In addition, we proposed an essential logic functionality "ERASE" based on spin transfer in a quasilinear molecular ion $[Fe\text{-}O\text{-}CO]^+$, a topological spin-charge gearbox on a real molecular magnet $Co_3Ni(EtOH)^+$, and a two-level qubit system with Dy and Ni atoms in $[Dy_2Ni_2(L)_4(NO_3)_2(DMF)_2]$ [45–48]. The developed on-chip integration technology provides a feasible way to integrate molecular spintronics on the compact and stable platform, such as graphene, graphene oxide, transition-metal dichalcogenides (TMDCs), and black phosphorus [49,50]. For instance, Sarkar *et al.* demonstrated the doping effect of MoS_2 by diverse metallic nanoparticles at the experimental level [51]. MoO_3 nanosheets were successfully deposited onto WSe_2 by a rapid flame synthesis method [52]. With respect to driving lasers, the on-chip-laser technology, such as a single-chip optical phased array [53–55] or a single-photon emitter [56], can be deemed as a promising solution to implement concurrent spin manipulations on magnetic molecular elements.

Here, we propose an ideal model of an integrated logic processor built from an array of single molecular spin logic units and the connection bridges among them. Using this idea, we can transform a complicated integrated logic system into several small building blocks. Basically, our model divides functionality into two parts: local (on-site) spin functionality, and global functionality (transfer of the information bit from

*liuj@physik.uni-kl.de
†lichun@nwpu.edu.cn
‡lefkidis@physik.uni-kl.de

one site to another). Local processes necessitate individual addressability (which governs the speed of logic processing and the density of processing units), while global ones require elementary processes with high tolerance against local environmental fluctuations demonstrated in our previous work (e.g., local geometry and a magnetic environment) [57,58]. Motivated by the intriguing magnetic properties of graphene [59–62] and our previous investigations on fullerenes [63–66], we unfolded the fullerene into a one-dimensional structure, we took the zigzag carbon chain (mimicking the zigzag boundary of graphene) with two Ni atoms attached as the example of building blocks, and we demonstrated the addressability of local spin flip on single Ni atoms and the feasibility of global spin transfer through a distance comparable to the size of current CMOS devices [57]. In this paper, we combine two carbon chain structures to form a carbon cross, and we investigate the global spin-transfer scenarios through the bent carbon chain structure and the single spin addressability. This is a further step beyond our previous investigations on the carbon chain, and it exhibits more complicated spin-dynamics scenarios on different geometric configurations. The present study is also a key component of our investigations of integrated logic processing units.

II. THEORY AND METHODS

The Hartree-Fock (HF) approximation is first used to obtain the molecular orbitals of the systems and generate the single-body Slater determinant. Then we take the HF ground determinant as the reference and use a highly correlated method to calculate the many-body wave function of the ground state, namely the coupled cluster singles and doubles (CCSD). On top of this, the equation-of-motion CCSD (EOM-CCSD) method is applied to find the correlated wave functions of excited states. We use the 6-31G basis set. Notably, due to the high computational cost, it is almost impossible to perform the full coupled-cluster calculations on such a large system. Therefore, we restrict ourselves to an active window for both CCSD and EOM-CCSD calculations, which includes all the d-character orbitals.

In our investigations, the spin-dynamics scenarios are dealt with a theoretical model called the "Λ process" [67–69]. The main idea of the Λ process is the population transition between two specific states via one or several intermediate states induced by an external femtosecond laser pulse. The Λ process consists of two steps: one is the excitation process from the initial state to the intermediate states, while the other is the deexcitation process from the populated intermediate states to the target state. By selecting appropriate spin states as the initial and target states, one can generate several specific spin-dynamics scenarios based on the Λ process. For example, if the spin density is localized on the same atom with opposite spin directions for the initial and target states, the Λ process is a spin-flip process; if the spin density is localized on two different atoms with the same spin direction for the initial and target states, a spin-transfer process is achieved. Although the Λ process is a two-photon process, it can be faster than the direct transition when the latter is forbidden. According to our previous results, the Λ processes are usually accomplished within a subpicosecond regime.

For achieving a Λ process, spin-orbit coupling (SOC) and an external magnetic field are required. SOC is involved to generate the spin-mixed intermediate states necessary for achieving the spin-flip processes, and the external magnetic field is applied to reduce the degeneracy among the initial and target states so that they can be distinguished. The corresponding Hamiltonian is

$$\hat{H}_{\mathrm{SOC\&B}} = \sum_{i=1}^{N_{\mathrm{el}}} \frac{Z_a^{\mathrm{eff}}}{2c^2 r_i^3} \hat{\mathbf{L}} \cdot \hat{\mathbf{S}} + \sum_{i=1}^{N_{\mathrm{el}}} \mu_{\mathrm{L}} \hat{\mathbf{L}} \cdot \mathbf{B} + \sum_{i=1}^{N_{\mathrm{el}}} \mu_{\mathrm{S}} \hat{\mathbf{S}} \cdot \mathbf{B}, \quad (1)$$

where N_{el} is the number of electrons, Z_a^{eff} is the relativistic effective nuclear charge of the ath atom, accounting for the two-electron contributions to SOC, c is the speed of light, and r_i^3 denotes the position of the ith electron. $\hat{\mathbf{L}}$ and $\hat{\mathbf{S}}$ are the orbital and the spin angular momentum operators, respectively. μ_{L} and μ_{S} are the corresponding gyromagnetic ratios. $\mathbf{B}$ is a static external magnetic field, which breaks the time reversal symmetry of the system, thus allowing for distinction between spin-up and spin-down states. The time-dependent interaction between the laser pulse and the many-body wave functions is described as

$$\hat{H}_{\mathrm{int}}(t) = \hat{\mathbf{D}} \cdot \mathbf{E}_{\mathrm{laser}}(t), \quad (2)$$

where $\mathbf{E}_{\mathrm{laser}}(t)$ is the time-dependent electric field of the laser pulse, and $\hat{\mathbf{D}}$ is the electric-dipole-transition operator. By simplifying the time-dependent Schrödinger equations, we obtain the coefficient of each involved many-body wave function as a function of time,

$$\frac{\partial c_n(t)}{\partial t} = -\frac{i}{\hbar} \sum_k \langle \Psi_n | \hat{H}_{\mathrm{int}}(t) | \Psi_k \rangle c_k(t) e^{-i(E_k - E_n)t/\hbar}, \quad (3)$$

where c_n is the coefficient of the many-body state $|\Psi_n\rangle$, which is obtained from CCSD and EOM-CCSD calculations and modified with the effect of SOC and the external magnetic field, and E_n is the energy of the many-body state $|\Psi_n\rangle$.

By using an embedded fifth-order Runge-Kutta method and the Cash-Karp adaptive-step-size control [70], the above differential equations are numerically solved. The parameters of the laser pulses are optimized with our own genetic algorithm program [71]. There are eight parameters involved in the optimization calculations: the angles of incidence in spherical coordinates (θ and ϕ), the angle between the polarization of light and the optical plane (γ), ellipticity (β), the full width at half-maximum of the laser pulse (FWHM), the laser energy (E_{laser}), the amplitude of the laser pulse, and the chirp, which indicates the linear sweep of the frequency (at times $\pm$FWHM) with respect to the peak (central) frequency. The ranges of θ and ϕ are from 0° to 180° and 0° to 360°, respectively. The range of γ is from 0° to 360°. The range of the FWHM is from 0 to 500 fs. The amplitude ranges from 0 to 5.14×10^7 V/m. The range of chirp is given from -5% to $+5\%$. Each laser pulse serves as one individual of one generation, and the eight parameters are the genes of this individual. A total of 200 individuals are taken in each generation, and about 200 generations are usually needed in the optimization. The quality of each individual is determined by its "fidelity," which is defined as the population of the target state after the influence of the laser pulse. We regard a Λ process with fidelity higher than 95% as successful. All the

TABLE I. The expectation values of spin density distributed on Ni_2C_{24} and Ni_2C_{44}. Energies and expectation values of the spin angular momentum components $\langle \hat{S}_z \rangle$ of the initial and target states of the spin-dynamic scenarios calculated by EOM-CCSD are listed as well. SOC and external magnetic field ($B = 0.235$ T, along the z axis) are included. The sign of $\langle \hat{S}_z \rangle$ denotes the spin direction: positive and negative values are spin-up and spin-down, respectively. The dominant virtual excitation denotes the excitation Slater determinant of the many-body states with the highest amplitude. The amplitude is the linear combination coefficient of the corresponding virtual excitation calculated by the CCSD and EOM-CCSD calculations.

				Spin density				
Structures	State	E (eV)	$\langle \hat{S}_z \rangle$	Ni1	Ni2	ECEs	Dominant virtual excitation	Amplitude
	$\|1\rangle$	0.000	−1.000	−0.064	−0.060	−1.220	$MO_{112} \rightarrow MO_{113}$	0.597
Ni_2C_{24}	$\|64\rangle$	3.880	−1.011	−0.824	−0.015	−0.947	$MO_{112} \rightarrow MO_{115}$	0.613
	$\|68\rangle$	4.007	−1.039	−0.024	−0.820	−0.957	$MO_{112} \rightarrow MO_{114}$	0.615
	$\|1\rangle$	0.000	−0.999	−0.026	−0.062	−0.537	$MO_{181} \rightarrow MO_{183}$	0.580
Ni_2C_{44}	$\|29\rangle$	2.235	−0.999	−1.553	−0.007	−0.107	$MO_{175} \rightarrow MO_{186}$	0.472
	$\|38\rangle$	2.784	−1.000	−0.010	−1.411	−0.193	$MO_{182} \rightarrow MO_{200}$	0.392

states obtained from the CCSD and EOM-CCSD calculations are included in the optimization.

III. RESULTS AND DISCUSSION

A. Spin-density distribution on carbon crosses

Figures 1(a) and 1(b) illustrate the geometric configurations of carbon cross structures with two Ni atoms attached. We denote such cross systems as Ni_2C_n, where n is the number of carbon atoms. The geometric parameters of the carbon cross are identical to those of carbon chain structures in our previous investigation [57]. The lengths of the C-C and the C-H bonds are 1.420 and 1.090 Å, respectively. The angle between two adjacent C-C bonds is 120°. Note that there are two additional carbon atoms in the center of the cross structure. The crossing through a single C atom is not possible without breaking the conjugacy of both chains, since the middle C atom would have an sp^3 hybridization. Besides the two additional atoms and the two common carbon atoms in the center, each edge contains $(n-4)/4$ carbon atoms. We take two structures of different sizes as examples (Ni_2C_{24} and Ni_2C_{44}), of which the single edge contains five and ten carbon atoms, respectively. The pure carbon cross structures belong to the symmetry group of C_{2h}, and the four carbon edges are identical. With two Ni atoms asymmetrically attached to the two edges, the symmetry is reduced to C_s. These two Ni atoms are denoted as Ni1 and Ni2, respectively. The two empty carbon edges are denoted as ECEs. Notably, if we take the carbon cross systems shown in Fig. 1 as the basic fragments of the aforementioned logic processing unit, the two ECEs can thus be regarded as the connection channels among the multiple fragments.

To achieve various spin-dynamics scenarios via the Λ process, states with proper spin density distribution scenarios are required: (i) states with the spin density highly localized on the Ni atoms (since the Ni atoms serve as the magnetic centers in our ideal logic processing unit model); and (ii) states with the spin density unequally distributed between two Ni atoms (otherwise one cannot distinguish the two Ni atoms in a spin-transfer process). The spin density distribution on each many-body state is described with the Mulliken population analysis. According to our calculations, the lowest state of Ni_2C_{24} that fulfills both requirements (i) and (ii) is a triplet state lying at 3.880 eV. The corresponding spin density is highly localized on Ni1 with an absolute value of 0.824, while the spin density on Ni2 is much less and its absolute value is only 0.015 (state $|64\rangle$ in Table I). The total spin density is around 2.000, and the remaining spin density is mainly distributed on the two ECEs and almost equally shared by each carbon atom. The unbalanced spatial distribution of spin density results from the asymmetric positions of the two Ni atoms. Near this triplet state, we find another triplet state lying at 4.007 eV, which has high spin localization on Ni2. The corresponding spin density is 0.820 on Ni2 and 0.024 on Ni1 (state $|68\rangle$ in Table I). The remaining spin density is also equally distributed on the carbon atoms of the two ECEs. In addition, we find that the ground state is also a triplet but exhibits spin localization on the two ECEs. The absolute values of the spin density on the two ECEs are 0.622 and 0.598 (state $|1\rangle$ in Table I), respectively. Thus this triplet state can serve as the initial (target) state if one takes the two ECEs as the spin input (output) bits. For Ni_2C_{44}, a similar case can be found: The ground state also exhibits spin localization on the two ECEs (state $|1\rangle$ in Table I). However, the states with spin density highly localized on the single Ni atom lie at lower energies compared to Ni_2C_{24}. For example, the triplet state at 2.235 eV has spin density with an absolute value of 1.553 localized on the Ni1 atom (state $|29\rangle$ in Table I), while the remaining spin density is mostly found on the carbon edge with Ni1 attached.

The spin-density distribution can be well explained by the delocalized electronic configuration of the ground state. The coupled-cluster many-body wave functions are the linear combination of a number of Slater determinants built from HF-optimized molecular orbitals (MOs). Except for the HF reference determinant, the other determinants contain virtual excitations from the occupied MOs to the unoccupied MOs. We take the lowest triplet state of Ni_2C_{24} as an example. The dominant virtual excitation of the ground triplet state is from MO_{112}, which is the highest occupied molecular orbital (HOMO), to MO_{113}, which is the lowest unoccupied molecular orbital (LUMO), with an amplitude of 0.597. MO_{112} is mainly composed of the p_z orbitals of the carbon atoms on the two ECEs. The degenerate p_z orbitals form a delocalized π orbital, as shown in Fig. 1(c). MO_{113} mainly

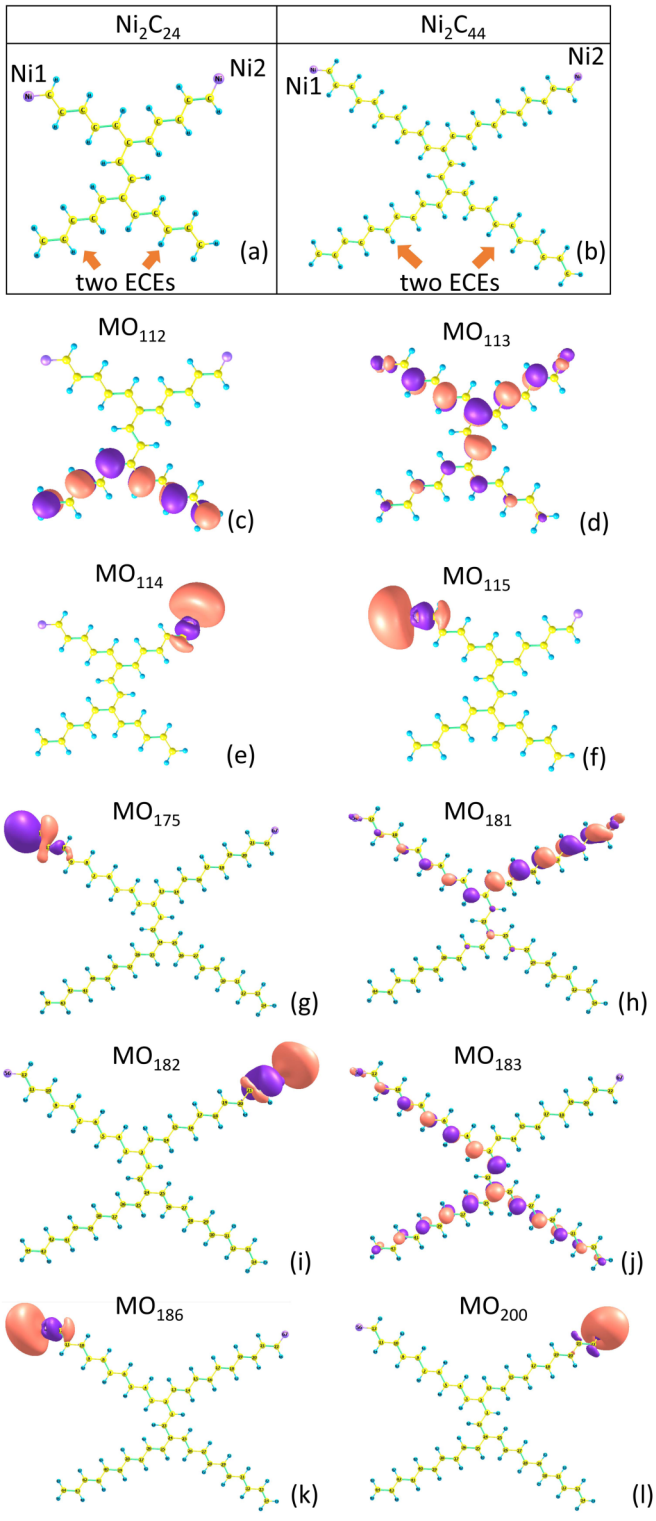

FIG. 1. The geometric configurations of (a) Ni_2C_{24} and (b) Ni_2C_{44}. The purple spheres denote the two Ni atoms, the yellow spheres denote the carbon atoms, and the blue spheres denote the hydrogen atoms. Panels (c)–(f) are the schematics of the molecular orbitals of Ni_2C_{24}: MO_{112}, MO_{113}, MO_{114}, and MO_{115}. Panels (g)–(l) depict the molecular orbitals of Ni_2C_{44}: MO_{175}, MO_{181}, MO_{182}, MO_{183}, MO_{186}, and MO_{200}.

consists of the delocalized π orbital of the carbon edges with the Ni atoms attached, as shown in Fig. 1(d). The singly occupied π orbitals consequently result in the magnetization of the carbon edges instead of the Ni atoms. As for the states with the spin density localized on a single Ni atom, it is because the MOs mainly contributed by the atomic orbitals of the corresponding Ni atom are included in the dominant virtual excitations. For example, for state $|64\rangle$, the magnetization mainly stems from the virtual excitation from MO_{112} to MO_{115}, which mainly consists of the atomic orbitals of Ni1. Notably, the contribution from MO_{112} explains the nonzero spin density distributed on the ECEs shown in Table I. As for state $|68\rangle$, the dominant virtual excitation is from MO_{112} to MO_{114}, which is mainly composed by the atomic orbitals of Ni2. Similar cases can be found on the larger Ni_2C_{44} structure. The corresponding dominant virtual excitation is shown in Table I as well. However, different from Ni_2C_{24}, the dominant virtual excitation takes place between the two MOs of the same atoms, such as MO_{175} and MO_{186}, which form the dominant Slater determinant of state $|29\rangle$. They are both composed of the atomic orbitals of Ni1. This explains why there is less spin localization on ECEs of states $|29\rangle$ and $|38\rangle$. The spin distribution of all the many-body states of Ni_2C_{24} and Ni_2C_{44} is given in Tables III and IV.

B. Spin-transfer scenarios on carbon crosses

Figure 2(a) illustrates the ideal model of an optical integrated logic unit leveraging the spin-dynamic processes of carbon cross structures. These processes can be divided into two scenarios: (i) global spin transfer through the carbon cross, and (ii) local spin flip on the single Ni atom. In our idea, the Ni atoms are employed as the most fundamental logic processing elements. The spin direction encodes the bit "1" by spin up and "0" by spin down. Therefore, the spin flips on the Ni atoms correspond to the simplest logic functionality, i.e., the NOT gate. Note that we do not regard the whole system as a two-qubit logic unit, but we consider the two Ni atoms as the separated logic units, and we are only focusing on the local spin flip and the global spin-transfer properties. The feasibility of the global spin-transfer processes allows the spin information transmissions between the two Ni atoms, integrating the Ni atoms into a large-scale circuit. Considering the spin localization and spin direction, there are 12 specific spin-transfer processes, including the spin transfer between two Ni atoms (Ni1 $\downarrow \rightarrow$ Ni2 $\downarrow$, Ni2 $\downarrow \rightarrow$ Ni1 $\downarrow$, Ni1 $\uparrow \rightarrow$ Ni2 $\uparrow$, and Ni2 $\uparrow \rightarrow$ Ni1 $\uparrow$), the spin transfer between Ni1 and ECEs (Ni1 $\downarrow \rightarrow$ ECEs $\downarrow$, ECEs $\downarrow \rightarrow$ Ni1 $\downarrow$, Ni1 $\uparrow \rightarrow$ ECEs $\uparrow$, and ECEs $\uparrow \rightarrow$ Ni1 $\uparrow$), and the spin transfer between Ni2 and ECEs (Ni2 $\downarrow \rightarrow$ ECEs $\downarrow$, ECEs $\downarrow \rightarrow$ Ni2 $\downarrow$, Ni2 $\uparrow \rightarrow$ ECEs $\uparrow$, and ECEs $\uparrow \rightarrow$ Ni2 $\uparrow$), where $\uparrow$ and $\downarrow$ denote the spin directions. Only triplet states are selected as the initial and the target states for the Λ process, since they allow for the separation of charge and spin dynamics.

Now let us focus on the spin-down-transfer processes on the Ni_2C_{24} structure. For the spin-transfer scenarios between Ni1 and Ni2, we choose the aforementioned states $|64\rangle$ and

TABLE II. Optimized parameters of the laser pulse for each spin-transfer and spin-flip process on the carbon cross system. ΔE is the energy difference between the initial and target states. θ and φ denote the angles of incidence in spherical coordinates, and γ is the angle between the polarization of the light and the optical plane. FWHM is the full width at half-maximum of the laser pulse, and E_{laser} denotes the laser energy. The chirp is linear, and the tabulated values indicate the change of the frequency at times ±FWHM with respect to the peak (central) frequency (zero means no chirp).

	Structure	Scenario	Fidelity (%)	ΔE (eV)	θ (deg)	φ (deg)	γ (deg)	Amplitude (10^9 V/m)	FWHM (fs)	E_{laser} (eV)	chirp (%)
spin transfer	Ni_2C_{24}	Ni1↓→ Ni2↓	92.9	0.127	100.0	18.9	0.5	1.757	309	0.127	+4.83
		Ni1↓→ ECEs↓	98.5	3.880	58.6	29.0	87.4	2.713	447	2.160	−2.31
		Ni2↓→ ECEs↓	99.1	4.007	94.9	16.1	213.1	1.316	475	3.920	+0.40
	Ni_2C_{44}	Ni1↓→ Ni2↓	99.9	0.549	128.3	183.9	47.8	0.140	226	0.535	−1.40
		Ni1↓→ ECEs↓	98.3	2.235	111.0	351.5	47.0	0.818	86	1.869	+3.92
		Ni2↓→ ECEs↓	99.9	2.784	92.3	88.7	33.7	1.552	323	2.696	+2.42
spin flip	Ni_2C_{24}	Ni1↓→ Ni1↑	92.9	0.113	53.7	116.7	290.0	4.011	296	1.340	0.00
		Ni2↓→ Ni2↑	86.5	0.113	61.0	74.5	321.7	4.238	456	2.163	0.00
	Ni_2C_{44}	Ni1↓→ Ni1↑	83.4	0.104	74.0	118.8	75.2	0.209	476	0.966	0.00
		Ni2↓→ Ni2↑	96.7	0.010	98.5	26.5	22.7	1.159	436	1.938	0.00

$|68\rangle$ as the initial and target states of the Λ process. If the system is excited from state $|64\rangle$ to state $|68\rangle$, a spin-transfer process from Ni1 to Ni2 is achieved. After the global optimization of the laser parameters with our genetic algorithm program, the fidelity reaches 92.9%. The corresponding laser parameters are listed in Table II, and the time evolution of the population of each many-body state is illustrated in Fig. 2(b). The whole transfer process finishes within about 450 fs. Such a process demonstrates that the two Ni atoms can still indirectly interact with each other through a bent long-distance carbon chain structure, which is a further improvement of our previous results on the linear carbon chain structure [57]. Notably, the reverse transfer process Ni2 → Ni1 is also achieved with the same laser pulse, except that the chirp is symmetrically modified from 4.83% to −4.83%. The fidelity of the reverse spin-transfer process reaches 90.4%, which is almost the same as in the forward process (see Appendix for details).

The reversibility actually results from two factors: one is that the same many-body states are populated during the two processes, and the other is that the original process ends with a comparably high fidelity. In contrast to the ERASE functionality [45], the chirp is applied to break the time-reversed symmetry so that one can fix the direction of the information transition. Both processes involve eight intermediate states, namely states $|1\rangle$, $|22\rangle$, $|25\rangle$, $|52\rangle$, $|57\rangle$, $|60\rangle$, $|61\rangle$, and $|63\rangle$. Most of them are practically pure-spin states (triplets) with spin component $\langle S_z\rangle = -1$. This is understandable since both the initial and the target states are pure spin-down states as well. The success of the long-distance spin transfer between the two Ni atoms is attributed to the conjugation effect on the carbon cross. Out of the eight intermediate states, states $|25\rangle$ and $|57\rangle$ play the most important role. If we delete either of these two states, the spin-transfer processes get almost completely suppressed, with fidelity lower than 40%. Both

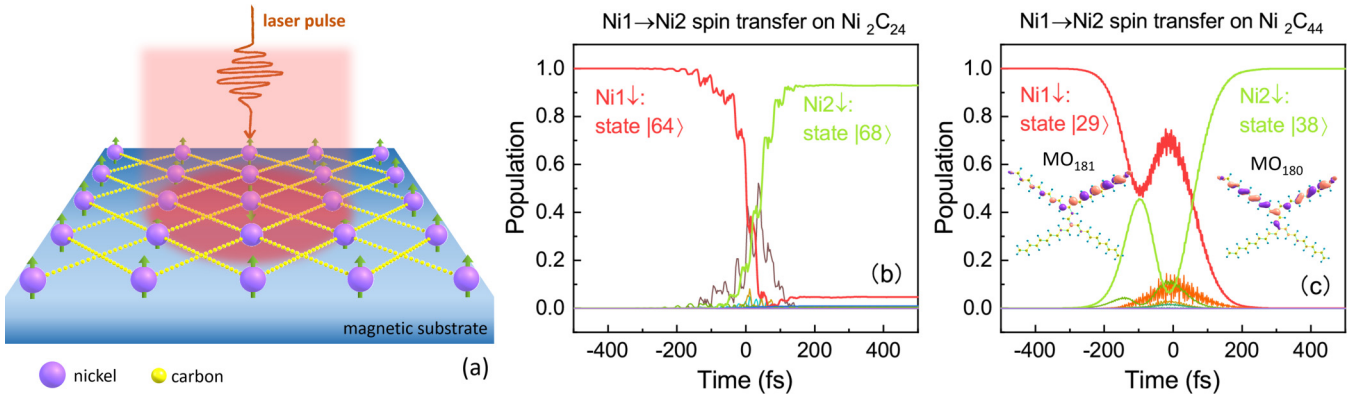

FIG. 2. (a) The schematic of an optical integrated spin logic unit assembled by multiple carbon cross structures. The purple and yellow spheres denote the nickel and carbon atoms, respectively. The spin (green arrows) states of each Ni atom are manipulated by the optomagnetic coupling field. The nickel atoms serve as the spin logic elements (spin flip) and the carbon atoms serve as the communication channels among the Ni atoms (spin transfer). (b) The Ni1 → Ni2 spin-transfer processes on Ni_2C_{24}. (c) The Ni1 → Ni2 spin-transfer processes on Ni_2C_{44}. The red lines denote the state with spin localized on Ni1 and the green lines denote the state with spin localized on Ni2. The lines in other colors denote the intermediate states. The two arrows ↓ and ↑ represent the spin direction of the corresponding states. The excitation $MO_{181} \rightarrow MO_{180}$ is the dominant excitation of the Ni1 → Ni2 spin-transfer processes on Ni_2C_{44}, which are shown in panel (c).

TABLE III. The expectation values of spin density distributed on Ni_2C_{24}. Energies and expectation values of the spin angular momentum components $\langle \hat{S}_z \rangle$ of all the many-body states calculated by EOM-CCSD are listed as well. SOC and external magnetic field ($B = 0.235$ T, along the z axis) are included. The sign of $\langle \hat{S}_z \rangle$ denotes the spin direction: positive and negative values are spin-up and spin-down, respectively.

			Spin density		
State	E (eV)	$\langle \hat{S}_z \rangle$	Ni1	Ni2	ECEs
$\|1\rangle$	0.000	−1.000	−0.064	−0.060	−1.220
$\|2\rangle$	0.000	0.000	0.000	0.000	0.000
$\|3\rangle$	0.000	1.000	0.064	0.060	1.220
$\|4\rangle$	0.913	0.000	0.000	0.000	0.000
$\|5\rangle$	1.240	0.000	0.000	0.000	0.000
$\|6\rangle$	1.449	−0.002	−0.002	−0.001	0.000
$\|7\rangle$	1.449	0.000	0.000	0.000	0.000
$\|8\rangle$	1.465	−0.002	−0.001	−0.002	0.000
$\|9\rangle$	1.466	0.000	0.000	0.000	0.000
$\|10\rangle$	1.479	0.002	0.002	0.001	0.000
$\|11\rangle$	1.496	0.002	0.001	0.002	0.000
$\|12\rangle$	1.519	−0.001	−0.001	−0.001	0.000
$\|13\rangle$	1.537	−0.001	−0.001	−0.001	0.000
$\|14\rangle$	1.564	0.002	0.001	0.001	0.000
$\|15\rangle$	1.564	0.000	0.000	0.000	0.000
$\|16\rangle$	1.582	0.000	0.000	0.000	0.000
$\|17\rangle$	1.582	0.002	0.001	0.001	0.000
$\|18\rangle$	1.911	0.000	0.000	0.000	0.000
$\|19\rangle$	1.917	0.000	0.000	0.000	0.000
$\|20\rangle$	1.930	0.000	0.000	0.000	0.000
$\|21\rangle$	1.935	0.000	0.000	0.000	0.000
$\|22\rangle$	1.951	−0.996	−0.150	−0.170	−0.505
$\|23\rangle$	1.951	0.000	0.000	0.000	0.000
$\|24\rangle$	1.951	0.996	0.150	0.170	0.505
$\|25\rangle$	2.171	−1.019	−0.133	−0.135	−1.107
$\|26\rangle$	2.171	0.000	0.000	0.000	0.000
$\|27\rangle$	2.171	1.019	0.133	0.135	1.107
$\|28\rangle$	2.484	−0.002	−0.001	−0.001	0.000
$\|29\rangle$	2.484	−0.217	−0.078	−0.083	−0.040
$\|30\rangle$	2.485	0.216	0.078	0.083	0.040
$\|31\rangle$	2.490	−0.294	−0.188	−0.189	−0.016
$\|32\rangle$	2.490	0.296	0.189	0.190	0.016
$\|33\rangle$	2.491	0.001	0.000	0.000	0.000
$\|34\rangle$	2.514	−0.636	−0.397	−0.335	−0.047
$\|35\rangle$	2.514	0.636	0.397	0.335	0.047
$\|36\rangle$	2.514	0.000	0.000	0.000	0.000
$\|37\rangle$	2.758	−0.002	−0.001	−0.001	0.000
$\|38\rangle$	2.760	−0.053	−0.031	−0.032	−0.002
$\|39\rangle$	2.762	0.047	0.028	0.029	0.002
$\|40\rangle$	2.765	−0.082	−0.029	−0.079	−0.002
$\|41\rangle$	2.766	0.004	0.003	0.003	0.000
$\|42\rangle$	2.766	0.084	0.030	0.080	0.002
$\|43\rangle$	2.778	−0.076	−0.044	−0.030	−0.011
$\|44\rangle$	2.779	0.001	0.000	0.001	0.000
$\|45\rangle$	2.779	0.076	0.044	0.030	0.011
$\|46\rangle$	2.799	0.000	0.000	0.000	0.000
$\|47\rangle$	2.800	−0.080	−0.075	−0.032	0.000
$\|48\rangle$	2.802	0.080	0.075	0.032	0.000
$\|49\rangle$	2.802	0.000	0.000	0.000	0.000
$\|50\rangle$	2.981	0.000	0.000	0.000	0.000
$\|51\rangle$	2.982	0.000	0.000	0.000	0.000
$\|52\rangle$	3.008	−0.998	−0.206	−0.222	−0.693
$\|53\rangle$	3.009	0.000	0.000	0.000	0.000
$\|54\rangle$	3.009	0.998	0.206	0.222	0.693
$\|55\rangle$	3.254	0.000	0.000	0.000	0.000
$\|56\rangle$	3.282	0.000	0.000	0.000	0.000
$\|57\rangle$	3.407	−1.000	−0.195	−0.208	−1.207
$\|58\rangle$	3.407	0.000	0.000	0.000	0.000
$\|59\rangle$	3.408	1.000	0.195	0.208	1.207
$\|60\rangle$	3.878	−0.003	−0.001	0.000	0.000
$\|61\rangle$	3.879	−0.907	−0.088	−0.083	−1.048
$\|62\rangle$	3.879	−0.001	−0.001	0.000	0.000
$\|63\rangle$	3.879	0.909	0.088	0.083	1.050
$\|64\rangle$	3.880	−1.011	−0.824	−0.015	−0.947
$\|65\rangle$	3.880	0.001	0.001	0.000	0.000
$\|66\rangle$	3.880	1.012	0.825	0.015	0.946
$\|67\rangle$	4.005	0.000	0.000	0.000	0.000
$\|68\rangle$	4.007	−1.039	−0.024	−0.820	−0.957
$\|69\rangle$	4.007	0.000	0.000	0.000	0.000
$\|70\rangle$	4.007	1.039	0.024	0.820	0.957
$\|71\rangle$	4.441	−1.000	−0.241	−0.232	−0.300
$\|72\rangle$	4.441	0.000	0.000	0.000	0.000
$\|73\rangle$	4.441	1.000	0.241	0.232	0.300

of them are dominated by the virtual excitation that contains the conjugated π orbitals of the carbon chains. As in our previous results on the single carbon chain structures [57], such conjugated orbitals directly interact with the d orbitals of both Ni atoms and build the spin channels between them.

The Ni1 $\downarrow \rightarrow$ ECEs $\downarrow$ and Ni2 $\downarrow \rightarrow$ ECEs $\downarrow$ transfer processes are also achieved with extremely high fidelities, which are 98.5% and 99.1%, respectively. For both scenarios, we take the ground state $|1\rangle$ with spin density mainly localized on the two ECEs as the target state. The Ni1 $\rightarrow$ ECEs transfer process is accomplished within around 1100 fs, while the Ni2 $\rightarrow$ ECEs transfer is much faster (600 fs) and more efficient (see Appendix for details). The reversed spin-transfer processes are also achieved with the same laser pulses (of course the sign of the chirp is changed). The parameters of the corresponding laser pulses are listed in Table II. States $|25\rangle$ and $|57\rangle$ are still the two most dominant intermediate states. The absence of any of them reduces the fidelity to lower than 47%. This once again indicates the importance of the conjugated orbitals of the carbon atoms.

Now we enlarge the carbon cross system to Ni_2C_{44}. Although the distance between the two Ni atoms is increased, the spin transfer between them is still achieved within half a picosecond. Here we use states $|29\rangle$ (with spin localized on Ni1) and $|38\rangle$ (with spin localized on Ni2) as the initial and the target states, respectively. Both Ni1 $\rightarrow$ Ni2 and Ni2 $\rightarrow$ Ni1 transfer directions achieve extremely high fidelities (99.9% and 99.8%). The laser parameters are listed in Table II. Notably, the energy difference between the two states is 0.549 eV, which matches the optimized laser energy 0.535 eV. The nearly equivalent energy indicates this spin-transfer scenario is a direct excitation process between the initial and the fi-

TABLE IV. The expectation values of spin density distributed on Ni_2C_{44}. Energies and expectation values of the spin angular momentum components of all the many-body states calculated by EOM-CCSD are listed as well. SOC and external magnetic field ($B = 0.235$ T, along the z axis) are included. The sign of $\langle \hat{S}_z \rangle$ denotes the spin direction: positive and negative values are spin-up and spin-down, respectively.

			Spin density		
State	E (eV)	$\langle \hat{S}_z \rangle$	Ni1	Ni2	ECEs
$\|1\rangle$	0.000	−0.999	−0.026	−0.062	−0.537
$\|2\rangle$	0.000	0.000	0.000	0.000	0.000
$\|3\rangle$	0.000	0.999	0.026	0.062	0.537
$\|4\rangle$	0.936	0.000	0.000	0.000	0.000
$\|5\rangle$	1.109	−0.038	−0.039	−0.001	−0.013
$\|6\rangle$	1.110	0.000	0.000	0.000	0.000
$\|7\rangle$	1.112	0.038	0.039	0.001	0.013
$\|8\rangle$	1.186	0.000	0.000	0.000	0.000
$\|9\rangle$	1.198	−1.044	−0.009	−1.010	−0.478
$\|10\rangle$	1.198	0.000	0.000	0.000	0.000
$\|11\rangle$	1.198	1.043	0.009	1.010	0.478
$\|12\rangle$	1.217	0.000	0.000	0.000	0.000
$\|13\rangle$	1.393	0.000	0.000	0.000	0.000
$\|14\rangle$	1.438	−1.042	−0.035	−1.021	−0.439
$\|15\rangle$	1.439	0.000	0.000	0.000	0.000
$\|16\rangle$	1.439	1.042	0.035	1.021	0.439
$\|17\rangle$	1.561	0.000	0.000	0.000	0.000
$\|18\rangle$	1.561	−0.014	−0.013	0.000	−0.005
$\|19\rangle$	1.568	0.014	0.013	0.000	0.005
$\|20\rangle$	1.710	0.000	0.000	0.000	0.000
$\|21\rangle$	1.805	0.000	0.000	0.000	0.000
$\|22\rangle$	1.859	−1.000	−0.060	−0.044	−1.023
$\|23\rangle$	1.859	0.000	0.000	0.000	0.000
$\|24\rangle$	1.859	1.000	0.060	0.044	1.023
$\|25\rangle$	1.947	0.000	0.000	0.000	0.000
$\|26\rangle$	2.110	−0.997	−0.281	−0.047	−0.659
$\|27\rangle$	2.110	0.000	0.000	0.000	0.000
$\|28\rangle$	2.110	0.997	0.281	0.047	0.659
$\|29\rangle$	2.235	−0.999	−1.553	−0.007	−0.107
$\|30\rangle$	2.235	0.000	0.000	0.000	0.000
$\|31\rangle$	2.235	0.999	1.553	0.007	0.107
$\|32\rangle$	2.511	−0.999	−0.114	−0.035	−0.613
$\|33\rangle$	2.511	0.000	0.000	0.000	0.000
$\|34\rangle$	2.511	0.999	0.114	0.035	0.613
$\|35\rangle$	2.739	−1.000	−0.037	−0.512	−0.451
$\|36\rangle$	2.739	0.000	0.000	0.000	0.000
$\|37\rangle$	2.739	1.000	0.037	0.512	0.452
$\|38\rangle$	2.784	−1.000	−0.010	−1.411	−0.193
$\|39\rangle$	2.784	0.000	0.000	0.000	0.000
$\|40\rangle$	2.784	1.000	0.010	1.411	0.193
$\|41\rangle$	2.914	0.000	0.000	0.000	0.000
$\|42\rangle$	3.258	0.000	0.000	0.000	0.000
$\|43\rangle$	3.410	0.000	0.000	0.000	0.000
$\|44\rangle$	3.414	−1.046	−0.033	−1.020	−0.471
$\|45\rangle$	3.414	0.000	0.000	0.000	0.000
$\|46\rangle$	3.414	1.046	0.033	1.020	0.471
$\|47\rangle$	3.499	−0.998	−0.151	−0.042	−1.003
$\|48\rangle$	3.499	0.000	0.000	0.000	0.000
$\|49\rangle$	3.499	0.998	0.151	0.042	1.003
$\|50\rangle$	3.696	−1.000	−0.446	−0.019	−0.450
$\|51\rangle$	3.696	0.000	0.000	0.000	0.000
$\|52\rangle$	3.696	1.000	0.446	0.019	0.450
$\|53\rangle$	3.825	0.000	0.000	0.000	0.000
$\|54\rangle$	3.899	−1.005	−0.218	−1.290	−0.340
$\|55\rangle$	3.899	0.000	0.000	0.000	0.000
$\|56\rangle$	3.899	1.005	0.218	1.290	0.340
$\|57\rangle$	3.944	0.000	0.000	0.000	0.000
$\|58\rangle$	4.143	0.000	0.000	0.000	0.000

nal state, which is quite similar to the OISTR mechanism [27,28]. Actually, if one removes the 15 intermediate states involved in the transfer process, the fidelity still remains at a large value around 90%. A similar scenario is found for the Ni2 → ECEs spin-transfer process ($|38\rangle \rightarrow |1\rangle$), which is also a direct excitation process. The energy of the optimized laser pulse (2.696 eV) matches the energy difference between $|1\rangle$ and $|38\rangle$ (2.784 eV). Deleting the intermediate states can only induce a minor change of the fidelity in the range of around 0.1% (the original fidelity is 99.9%). Contrary to the previous one, the Ni1 → ECEs spin-transfer process proceeds as a Λ process. The initial and target states are $|29\rangle$ and $|1\rangle$, respectively. The energy difference between the two states (2.235 eV) is about 1.2 times the laser energy (1.869 eV), which indicates the importance of the intermediate states. Actually, with the absence of the two dominant intermediate states $|26\rangle$ and $|35\rangle$, the fidelity drops to 3.0% and 5.3%, respectively. The reverse spin-transfer proceeds similarly (with the chirp sign changed). The corresponding detailed illustrations are given in the Appendix.

These results are quite interesting since only the scenarios taking state $|38\rangle$ as the initial or target states are direct excitation processes. This can be explained by the oscillator strength among these states. Figure 3 depicts the optical spectra corresponding to the three states $|1\rangle$, $|29\rangle$, and $|38\rangle$. Since states $|1\rangle$ and $|29\rangle$ have higher oscillator strength with states $|26\rangle$ and $|35\rangle$ than with each other [shown in Figs. 3(a) and 3(b)], the states $|26\rangle$ and $|35\rangle$ are populated first during the spin-transfer process between Ni1 and ECEs. However, state $|38\rangle$ exhibits much lower oscillator strength with the mentioned two intermediate states but comparably higher interaction with $|1\rangle$ and $|29\rangle$ [shown in Fig. 3(c)], thus it more likely turns out to be a direct excitation process rather than a Λ process. One may also notice the high peak close to $|35\rangle$ from the left [shown in Figs. 3(a) and 3(c)], which results from the transition to state $|32\rangle$. Since this is off-resonant with the laser pulse, the influence from this state is negligible. In addition, the direct excitation is also attributed to the conjugated π orbitals of the carbon atoms. Taking the Ni1 → Ni2 spin-transfer process as an example, the initial and the target states both contain plenty of the virtual excitations involving the conjugated orbitals (MO_{181}). The interaction between MO_{181} and MO_{180}, which is another MO mainly composed of the π orbitals, contributes the most to the transition moment between the two states. The corresponding one-electron reduced density matrix (1eRDM) element of these two MOs is around 0.046, which is the largest element of the matrix. Therefore, although the dominant d

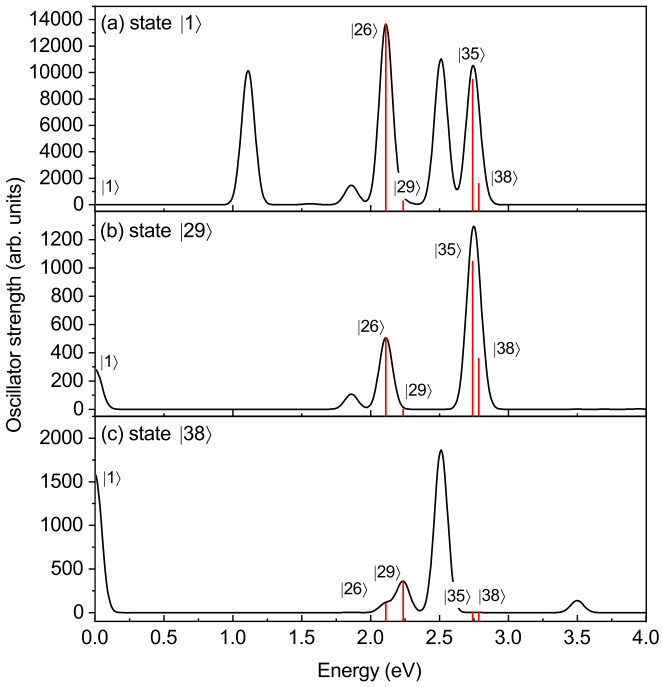

FIG. 3. The optical spectra of states $|1\rangle$ (a), $|29\rangle$ (b), and $|38\rangle$ (c) of Ni_2C_{44}. The red vertical lines mark the positions of the important states ($|1\rangle$, $|26\rangle$, $|29\rangle$, $|35\rangle$, and $|38\rangle$) involved in the spin-transfer processes.

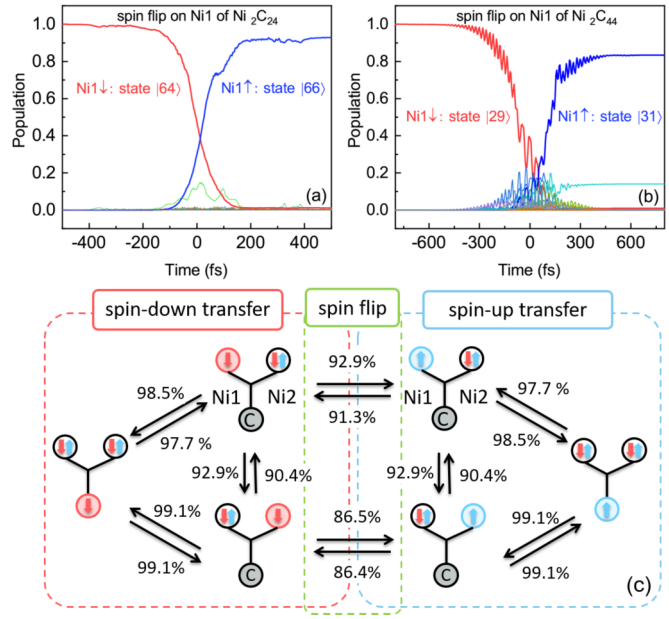

FIG. 4. The down-to-up spin-flip processes on the Ni1 atom of Ni_2C_{24} (a) and Ni_2C_{44} (b), respectively. The red and blue lines denote the time evolution of the population of the spin-down initial ($|64\rangle$ and $|29\rangle$) and spin-up target states ($|66\rangle$ and $|31\rangle$), respectively. The intermediate states are denoted by the lines in other colors. (c) Schematic of a complete spin transmission cycle based on the achieved spin-flip and spin-transfer processes. The red and blue arrows denote the spin direction and spin localization of the two Ni atoms. The gray circles with "C" inside denote the two ECEs with nearly zero spin density. The percentage values near the black arrows denote the fidelity of the spin-dynamic processes on Ni_2C_{24}.

orbitals of the two different Ni atoms cannot directly interact with each other, the conjugated π orbitals can still serve as the spin channels and transfer spin density from one Ni atom to the other. Moreover, our calculations show that the charge density on each C atom remains practically unchanged, which indicates a nondissipative charge-transfer process with the carbon cross serving as the conducting channel.

In the aforementioned spin-transfer processes, both the initial and the target states are the spin-down substates ($\langle S_z\rangle = -1$) of triplet states. If we take the corresponding spin-up states ($\langle S_z\rangle = +1$) as the initial and the target states, the spin-up transfer processes are achieved. For Ni_2C_{24}, the spin-up states $|3\rangle$, $|66\rangle$, and $|70\rangle$ correspond to the aforementioned spin-down states $|1\rangle$, $|64\rangle$, and $|68\rangle$, respectively. For Ni_2C_{44}, the spin-up states $|3\rangle$, $|31\rangle$, and $|40\rangle$ correspond to the aforementioned spin-down states $|1\rangle$, $|29\rangle$, and $|38\rangle$, respectively. Notably, one also finds the spin-up states corresponding to the spin-down intermediate states. The detailed information of these states is shown in Tables III and IV. Since the spin-up and the spin-down states stemming from the same triplet state have the same electronic configurations, the same laser pulses for driving the spin-down transfer processes can induce the spin-up transfer processes as well. Therefore, all the aforementioned 12 spin-transfer scenarios are achieved.

C. Spin-flip scenarios on carbon crosses

In this section, we introduce the local spin-flip scenarios on the two Ni atoms. The spin flips on the two ECEs are not taken into account, since they only serve as the input and output bits. Considering the spin localization and spin direction, there are in total four different cases: Ni1 $\downarrow \rightarrow$ Ni1 $\uparrow$, Ni1 $\uparrow \rightarrow$ Ni1 $\downarrow$, Ni2 $\downarrow \rightarrow$ Ni2 $\uparrow$, and Ni2 $\uparrow \rightarrow$ Ni2 $\downarrow$ (simultaneous spin-flip and spin-transfer is generally not found). The substates with opposite directions stemming from the same triplet state can be employed as the initial and target states of the spin-flip processes.

For the smaller structure Ni_2C_{24}, we directly choose states $|64\rangle$ and $|66\rangle$ as the initial and target states to achieve the spin flip on Ni1, and we choose states $|68\rangle$ and $|70\rangle$ for the spin flip on Ni2 (down-to-up spin-flip processes). For both, the energy differences between the two substates are 0.113 meV, which are large enough to make them addressable with a laser pulse and at the same time small enough to prolong the lifetime of the energetically higher state by suppressing the direct relaxation processes [72]. The highest fidelities of the spin flips on Ni1 and Ni2 reach 92.9% and 86.5%, respectively. Different from the spin-transfer processes, since the direct excitation between the initial and target states is electric-dipole forbidden (they are nearly pure spin states), spin-mixed intermediate states are required to serve as the population-transfer channels. Figure 4(a) illustrates the time-dependent population for the spin flip on the Ni1 atom of Ni_2C_{24}. Out of the 45 intermediate states, seven states are dominant. By deleting any of them, the fidelity is reduced to less than 35.0%. All of them are spin-mixed states (two of them are singlet states and the remaining ones are the $|S_z\rangle = 0$ substates of the triplets). Similar scenarios are found for the spin-flip process on the Ni2 atom. The reverse scenarios from

spin up (initial states: $|66\rangle$ and $|70\rangle$) to spin down (target state: $|64\rangle$ and $|68\rangle$) are also achieved with the same laser pulses. The corresponding fidelities are 91.3% (flip on Ni1) and 86.4% (flip on Ni2), respectively. Since the same laser pulses are used, the behavior is nearly identical to the original $|\downarrow\rangle \rightarrow |\uparrow\rangle$ spin flips (see Appendix for details). The mechanism of the reversibility of the spin-flip process is slightly different from the spin-transfer scenario: Due to the high similarity of the electronic configurations of the initial and target states, they exhibit nearly the same transition properties as the intermediate states, which ensures the spin-flip reverse. This is also the reason why the spin-flip process is reversible, but with comparably small fidelity.

For the larger carbon cross structure Ni_2C_{44}, the spin-down state $|29\rangle$ and the corresponding spin-up state $|31\rangle$ are used for achieving the spin flip on Ni1 [Fig. 4(b)]. The spin-down state $|38\rangle$ and the spin-up state $|40\rangle$ are chosen for the spin flip on Ni2. The fidelities of the $|\downarrow\rangle \rightarrow |\uparrow\rangle$ scenarios on Ni1 and Ni2 reach 83.4% and 96.7%, respectively. The reversed $|\uparrow\rangle \rightarrow |\downarrow\rangle$ flip scenarios are also accomplished with the same laser pulses. The corresponding fidelities on Ni1 and Ni2 are 81.2% and 96.2%, respectively. Each spin-flip process takes around 800 fs. Similar to the spin-flip scenarios on the Ni_2C_{24} structure, all dominant intermediate states are spin-mixed states. Since the spin-mixed states are necessary for achieving spin-flip processes on single magnetic centers, one can block a spin-flip process by hindering of the intermediate states, as will be discussed in the next section. Now we conclude that the spin-flip processes can be achieved on the magnetic centers of the carbon cross structures. Combined with the spin-transfer processes mentioned in the preceding section, we are able to form a complete spin information transmission cycle [shown in Fig. 4(c)]: one can modify the spin properties of the arbitrary spin centers (Ni1 and Ni2) and transfer the spin density along any arbitrary path (Ni-to-Ni, Ni-to-ECEs, and ECEs-to-Ni) with arbitrary spin direction (up or down). Additionally, considering that the laser pulses are short enough, these dynamic scenarios that start from pure states are inherently spin-coherent.

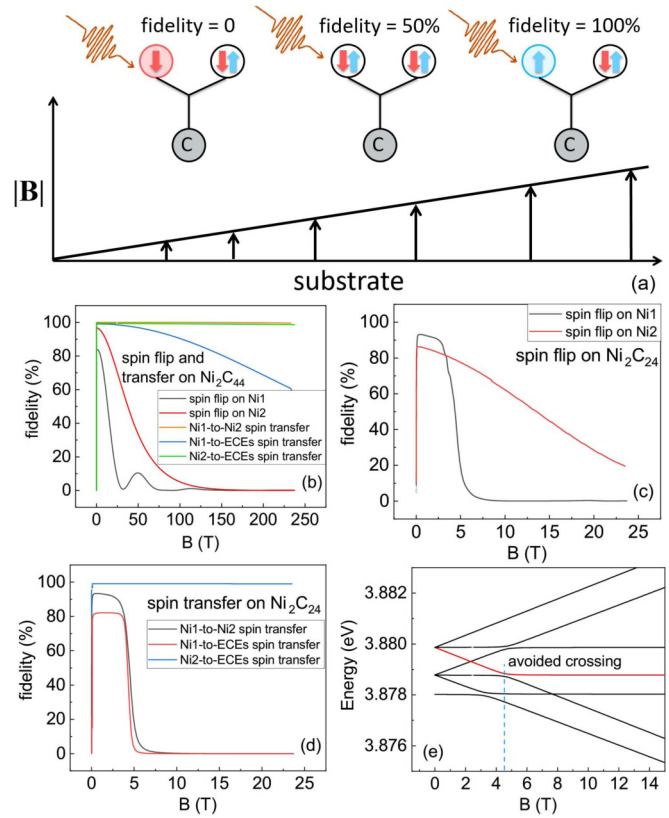

FIG. 5. (a) Schematic of magnetic field modulated spin-flip processes on a carbon cross system. The red and blue arrows denote the spin direction and spin localization of the two Ni atoms. The two ECEs are denoted by the gray circles. Only at the specific magnetic field strength is the spin flip achieved. In other words, the corresponding fidelity is 100%. (b)–(d) The dependence of local spin-flip and global spin-transfer processes of Ni_2C_{24} and Ni_2C_{44} on magnetic field strength, respectively. (e) The energy of the state $|64\rangle$ (red line) and its nearest states (black lines) at different magnetic field strength. The lowest state $|60\rangle$ at 0 T is a singlet state. The blue dashed line marks the avoided crossing between state $|64\rangle$ and state $|62\rangle$.

D. Individual spin addressing

In an integrated logic processor, the high addressability of a single spin center is required, e.g., Bayliss *et al.* demonstrated the optical addressability of ground-state spins in a series of synthesized organometallic, chromium (IV) molecules [73]. To the best of our knowledge, the minimum focal spot size of laser pulses reaches tens of nanometers [74,75], which is still larger than our system by one order of magnitude. Using laser pulses to address individual magnetic centers may fail since one on-chip pulse could spot on several spin centers in the meantime if they are densely arranged [57,58]. Considering that the Λ process can only be achieved with high fidelity under a specific magnetic field strength, we propose that one can use an inhomogeneous magnetic field to address the single spin centers (Ni atoms) on the carbon cross structure [Fig. 5(a)]. In principle, with the magnetic field strength increasing from 0 T, the fidelity of the local spin-flip process will first increase up to a maximum value for the magnetic field for which it was optimized, and then decrease. Since the optimization of the laser pulse is performed with the magnetic field strength of 0.235 T, the fidelity usually peaks at this value. When we increase the magnetic field strength from 0 to 0.235 T, the Zeeman effect gets enhanced, and the spin-mixed initial and target states (due to SOC) tend to be spin-pure and more addressable for the laser pulse. Therefore, the fidelity of the local spin-flip process increases (a similar scenario happens for spin-transfer processes). However, if we keep increasing the magnetic field, the SOC becomes relatively weak (Paschen-Back effect) and the dominant spin-mixed intermediate states also tend to be spin-pure, which, in turn, blocks the population-transfer channels and suppresses the spin-flip process. Notably, the spin-transfer processes preserve their high fidelity even for strong magnetic fields (> 0.235 T), because the pure-spin intermediate states turn out to be the major channels in such cases. This is also expected for preserving spin information during the transfer processes.

Figure 5(b) illustrates the magnetic-field-modulated fidelity of a local spin-flip process on the Ni1 atoms and the two

spin-transfer processes (Ni1 → Ni2 and Ni1 → ECEs) on Ni_2C_{44}. We stipulate that the Λ process fails if the corresponding fidelity is lower than 50%. For the spin-flip process on Ni1, the fidelity peaks at around 1.145 T and decreases down to 49.7% at around 11.870 T. Supposing that there are two neighboring carbon cross structures and the magnetic field gradient is 10 T/μm [76–81], the distance between the identical Ni1 atoms of the two crosses should be at least 1.073 μm [(11.870 − 1.145)/10] in order for the spin-flip scenarios to be distinguishable. Notably, Ni1 and Ni2 on the same carbon cross are distinguished according to the asymmetry configuration. The fidelity of the spin flip on Ni2 peaks at around 0.205 T and decreases to 49.0% at around 38.313 T. The corresponding distance between the two identical Ni2 atoms is 3.811 μm [(38.313 − 0.205)/10]. For the spin-transfer scenarios (between Ni1 and Ni2, and between Ni2 and ECEs), the fidelities are preserved after the process reaches the highest values. A special scenario occurs during the spin transfer between Ni1 and ECEs: the fidelity decreases slightly when the magnetic field strength exceeds 0.235 T. This is because two spin-mixed states $|5\rangle$ and $|7\rangle$ are involved as the intermediate states. The absence of them will decrease the fidelity to 85.4% and 86.4%, respectively. A strong magnetic field changes their electronic configurations and therefore slightly decreases the fidelity. Nevertheless, since the two spin-pure states $|26\rangle$ and $|35\rangle$ are the most important intermediate states, they ensure the high fidelity of the whole processes. According to our calculations, even if we increase the magnetic field to an unreasonably high value at 235.05 T, the fidelity is still higher than 60%.

The situations are a little bit different for the smaller structure Ni_2C_{24}. Especially for the spin-dynamics processes on Ni1, the fidelity drops abruptly at around 4.678 T [shown in Figs. 5(c) and 5(d)]. The whole processes, even the spin-transfer processes, are completely blocked when the magnetic field strength is larger than 8.490 T, which is much smaller than the corresponding strength on the larger system. This is attributed to the coherent superposition of the initial state and its quasidegenerate state induced by the SOC effect. For both spin flip on Ni1 and spin transfer from Ni1 to ECEs, we take state $|64\rangle$ as the initial state. Figure 5(e) depicts the energy levels of the state $|64\rangle$ (red line) and its six neighboring states. At 4.678 T (marked with the blue dashed line), there is an avoided crossing between the states $|64\rangle$ and $|62\rangle$, which means that there exists a coherent superposition of them. The electronic configuration of the initial state $|64\rangle$ changes, thus reducing the fidelity of the corresponding spin-dynamic processes. Based on these results, we give an additional conclusion that the SOC effect can further increase the sensitivity of the local spin flip with respect to the external magnetic field.

E. Double-pulse induced spin dynamics

Based on the results in the preceding section, the distances for distinguishing the local spin dynamics by using the inhomogeneous magnetic field are still much larger than the present CMOS scale (around 5 nm). Considering that the laser-induced spin-dynamic processes strongly depend on the quantum coherence of the involved many-body states, one can use a second pulse to manipulate the efficiency of the Λ process and thus increase the addressability of the local spin-flip processes. The second pulse is effective only with the specific relative phases induced by the first pulse. Such a process is termed the "double-pulse" process. Equations (3) become

$$\frac{\partial c_n(t)}{\partial t} = -\frac{i}{\hbar}\sum_k \langle\Psi_n|[\hat{H}_{\text{int1}}(t) + \hat{H}_{\text{int2}}(t+\Delta t)] \times |\Psi_k\rangle c_k(t) e^{-i(E_k - E_n)t/\hbar}, \tag{4}$$

where Δt is the delay between two laser pulses. $\hat{H}_{\text{int1}}(t)$ and $\hat{H}_{\text{int2}}(t)$ denote the interaction Hamiltonians of the first and the second pulses. Here we use the same initial and target states, and we apply the same external magnetic field used in the aforementioned single-pulse processes for the optimization of laser pulse parameters. The spin-flip scenario on the Ni1 atom of the larger structure Ni_2C_{44} is taken as the examples. As shown in Fig. 6(a), the first laser pulse cannot induce a complete spin flip from state $|29\rangle$ to state $|31\rangle$, but it results in a coherent quantum superposition of the involved states $\sum_i c_i(t_1)|\Psi_i\rangle e^{-i\omega_i t_1}$ (t_1 is the end time of the first laser pulse; ω_i is the energy difference between the ith state and the ground state). Before applying the second laser pulse, the phase of each state keeps rotating with the frequency of ω_i. After the time delay Δt, the proper relative phases are reached, and the second pulse is applied immediately to complete the spin flip. Figure 6(b) depicts the double-pulse spin flip on Ni1 with delay between the two laser pulses twice their FWHM. Its fidelity is 81.9%, which is similar to the value of the single-pulse spin-flip process. The parameters of the optimized laser pulse are $\theta = 31.9°$, $\phi = 53.7°$, $\gamma = 284.1°$, amplitude = 2.548×10^9 V/m, FWHM = 451 fs, $E_{\text{laser}} = 3.254$ eV, and chirp = −3.21%. Notably, the time delay Δt plays an important role for resulting in the high fidelity. If we fix the magnetic field strength (0.235 T) and change the delay, the spin-flip process can be completely blocked [shown in Fig. 6(c)].

Because the spin-mixed intermediate states still play the most important roles, one can use an inhomogeneous magnetic field to distinguish the local spin-flip processes on the two identical Ni atoms as well. Considering that ω_i is roughly proportional to the magnetic field strength $\omega_i(|\mathbf{B}|) \approx \omega_{0i} + \mu_i|\mathbf{B}|$ (ω_{0i} and μ_i are the energy and the magnetic moment of the ith state at 0 T), increasing of the magnetic field strength should result in an oscillation of the fidelity. Figure 6(d) shows the fidelity of the double-pulse spin-flip processes on Ni1 for different magnetic field strengths, exactly as we expect. These results are quite important, since they demonstrate that the double-pulse spin dynamics is more sensitive to the strength of the external magnetic field. Therefore, one can distinguish the local spin-flip processes on the two identical Ni atoms at shorter distances. Assuming that the gradient of the magnetic field strength is 10 T/μm, the shortest distance between the two identical Ni1 atoms has to be around 60.0 nm. Now we come to the conclusion of this section that double pulses can increase the individual addressability of the local spin flip and thus enhance the spatial resolution of the integrated spin logical devices that we mentioned.

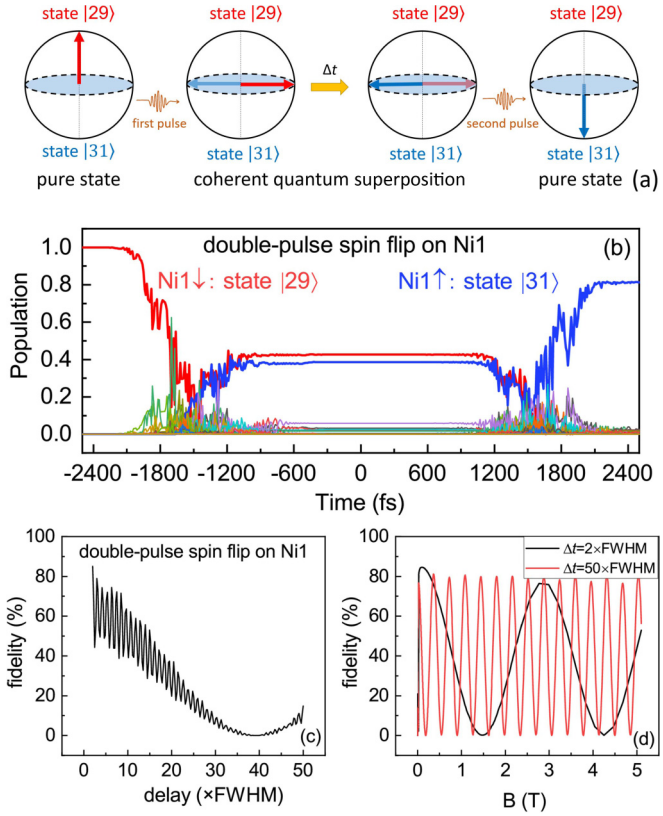

FIG. 6. The double-pulse-induced spin-flip processes on Ni1 of Ni_2C_{44}. (a) Schematic of the double-pulse-induced spin-flip dynamics. The arrows indicate the instantaneous states of the system. The system stays at the initial state $|29\rangle$ in the beginning. After the first pulse, the system is transferred to a coherent superposition state. After the delay Δt, the second pulse is active. The population is subsequently transferred to the target state $|31\rangle$. Panel (b) depicts the time evolution of the population of the initial, target, and intermediate states with a delay between the two pulses of two times the FWHM. Panel (c) depicts the fidelity of the double-pulse spin flip on Ni1 with a different delay between two laser pulses. Panel (d) depicts the corresponding fidelity of the spin-flip scenarios under the different magnetic field with a delay of two times (black line) and 50 times the FWHM (red line), respectively.

The fidelity of the second laser pulse depends on the phase of each involved state at $t_1 + \Delta t$, which is roughly $(\omega_{0i} + \mu_i|\mathbf{B}|)(t_1 + \Delta t)$. If we increase Δt, the phase will rotate more with respect to the magnetic field strength $|\mathbf{B}|$. Therefore, the spin-flip processes will be more sensitive to the magnetic field, and more oscillations will appear in the fidelity. Based on that, we further increase the spatial resolution for the local spin-flip processes by tuning the delay between the two pulses. According to our calculations, the distance between the two identical Ni1 atoms can be reduced to 5.8 nm if we set the time delay to 50 times the FWHM [shown in Fig. 6(d)]. Similar situations are found during the double-pulse spin-flip process on Ni2. The corresponding results are shown in the Appendix.

F. Effect of the direction of the laser pulse

Since the carbon cross structures exhibit anisotropic magnetic properties, applying laser pulses along different directions should, in principle, result in significant differences of the spin-dynamic processes. The propagation direction of the laser pulse is described by the polar angle θ and the azimuthal angle ϕ in spherical coordinates [shown in Fig. 7(a)]. In our previous investigations, we have discussed the modification scenarios of the spin-dynamics processes by changing the polar angle within a fixed tolerance [82]. Substantial drops of fidelity were observed for rotations of the laser pulse away from its optimal direction by a small angle (5°–10°). However the influence of the azimuthal angle ϕ was not investigated. Therefore, in this section, we take a step further and discuss the coupled effect of θ and ϕ on the aforementioned ultrafast spin-dynamic processes by varying them within a complete angle range (from 0° to 360°).

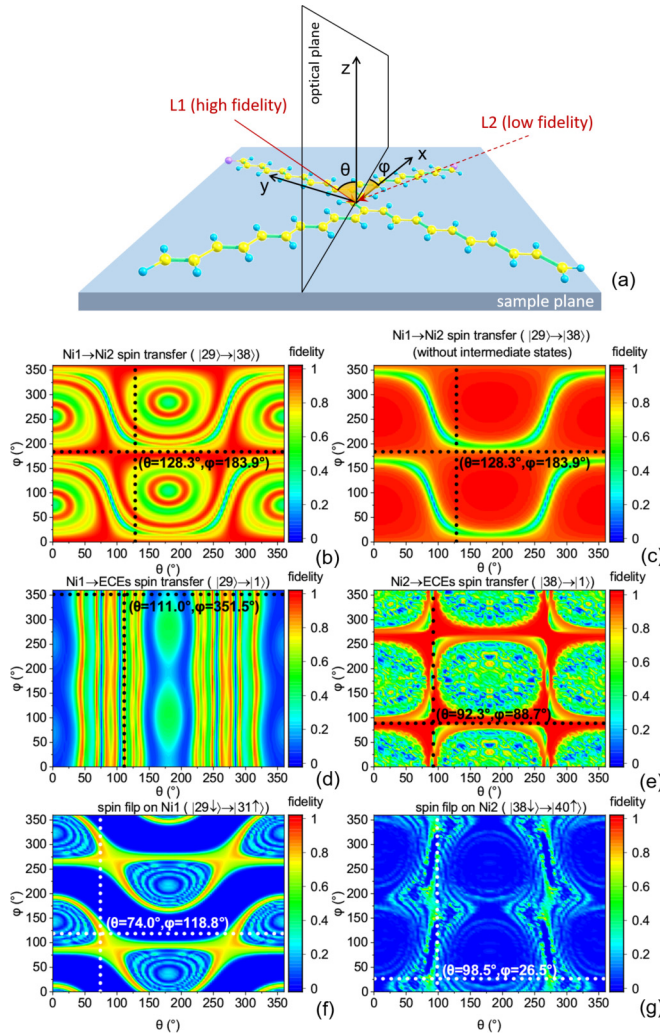

FIG. 7. (a) Schematic of the propagation directions of the applied laser pulses. L1 (red-solid arrow) and L2 (red-dashed arrow) are the laser pulses applied from different directions. L1 induces the high fidelity of the spin dynamics, while L2 induces low fidelity. θ and ϕ are the polar and azimuthal angles of L1, respectively. Panels (b)–(g) depict the fidelity of the spin-transfer and spin-flip processes on Ni_2C_{44} with different laser directions. The crossover point of the two dashed lines in each panel denotes the resonant direction of the laser pulse optimized by our genetic algorithm program.

The larger system Ni_2C_{44} is taken as the example. We fix the magnetic field strength to 0.235 T and all the parameters of the optimized laser pulses except for their polar angle and azimuthal angle. We increase the two angles from 0° to 360° with the step size of 3.6° (100 × 100 grid) and recalculate the fidelity of all aforementioned spin-dynamic scenarios for each laser direction. Figure 7 depicts the change of the local spin-flip and global spin-transfer fidelity by modifying θ and ϕ of the laser pulse. Since the polar angle ranges from 0° to 180°, the extended part ($180° < \theta < 360°$) is simply the reflection of the original panel. Notably, when θ is 0°, one can still find that the fidelity oscillates with the rotation of the azimuthal angle ϕ. This is due to the fact that the laser pulses are elliptically polarized. The elliptical polarization also results in the periodic change of fidelity along the ϕ axis with the period of 180°. In addition, each panels exhibits inversion symmetry about the points (90°, 90°), (90°, 270°), (270°, 90°), and (270°, 270°).

For each scenario, the deviation of the laser pulse from the resonant direction can result in a substantial change of the fidelity. For spin-transfer scenarios, one can find wider tolerance regions for reaching high fidelity than for the spin-flip scenarios. Especially for the two direct-excitation processes [Fig. 7(b) Ni1 → Ni2, Fig. 7(d) Ni1 → ECEs], a tolerance of around 25° from the optimized angles is found, which is the maximum value among all the scenarios. To understand these phenomena better, we delete all the intermediate states of the Ni1 → Ni2 process and perform the calculations again [Fig. 7(c)]. From nearly all the possible directions, the optimized laser pulse can induce a high fidelity for this transfer scenario. Such a fidelity conservation regarding the laser direction is attributed to the direction-independent large oscillator strength between the initial and target states. As we mentioned in the previous section, such a spin transfer mainly stems from the excitation $MO_{181} \rightarrow MO_{180}$. These two MOs are nearly uniformly distributed on the two carbon branches with the Ni attached, which results in large transition moments along both x and y axes. If we include the intermediate states, a large annular area and a small round area with low fidelity appears. Within this area, the population of the initial state $|29\rangle$ is substantially transferred to the intermediate state $|35\rangle$. This is also understandable due to the strong oscillator strength between the state $|35\rangle$ and the state $|29\rangle$ (Fig. 3). The same situation is also found for the Ni2 → ECEs transfer process. In addition, since spin transfers on the carbon cross structure are in-plane scenarios, the deviation of θ from the optimal value usually results in a drastic change of the fidelity. This is quite apparent for the Ni1 → ECEs transfer scenario [Fig. 7(d)]. For the spin-flip processes, since more intermediate states are involved, the competition between the intermediate states and the target states becomes even stronger. Therefore, a minor change of the polar angle or the azimuthal angle can result in a substantial drop of the fidelity. Similar scenarios are found in the smaller structure Ni_2C_{24}, and the corresponding results are shown in the Appendix.

IV. CONCLUSION

In summary, we systematically investigate the laser-induced ultrafast spin-dynamic processes on two different carbon cross structures with two Ni atoms attached (Ni_2C_{24} and Ni_2C_{44}) as well as the addressability of the local spin flip on each Ni atom. The high-level quantum chemistry theory CCSD and EOM-CCSD are used to calculate the electronic configurations of the ground and excited states of the systems. The spin density distributions are analyzed in detail based on the obtained many-body states. There are mainly three different distribution situations, namely spin localized on the two ECEs at low energy levels, and spin localized on Ni1 or Ni2 at high energy levels. By taking these states as the initial or target states and applying the well-optimized laser pulses, local spin flip on the two Ni atoms and the global spin transfer through the carbon crosses are theoretically achieved within the subpicosecond regime. Notably, the spin-transfer processes between the two Ni atoms demonstrate the possibility of an indirect interaction between the two Ni atoms through the carbon cross structure.

The modification scenarios of the external magnetic field on the spin-dynamic processes are investigated to prove the feasibility of individual spin addressability with Λ processes. We find that a magnetic field gradient can clearly distinguish the local spin-flip processes under the same laser pulses and in the meantime preserve the spin-transfer processes. This is crucial in real integrated circuits, in which the two processes must be separately controllable. In addition, the SOC effect suppresses the spin-dynamics processes on the smaller carbon cross Ni_2C_{24} by inducing the avoided crossing between the initial and the intermediate state, which is energetically close to the initial state. We present the interactions between the double pulses and the carbon crosses, and we find that a double-pulse propagation can further increase the sensitivity of the local spin flip with respect to the external magnetic field, which in turn increases the spatial resolution.

Finally, we investigate the effect of the laser direction on the spin-dynamic processes, and we find that the deviation of the laser pulse from the resonant direction can result in substantial changes on the spin-flip and spin-transfer processes. These investigations are a significant step beyond our previous research on the linear carbon-chain structures. They demonstrate a clearer picture for generating a more complete and complicated logic processing unit based on ultrafast optical spin dynamics and magnetic molecules in the future.

ACKNOWLEDGMENTS

We acknowledge financial support from the National Natural Science Foundation (Grants No. 11872309, No. 12172293, No. 11572251, and No. 11504223) of China and the Natural Science Basic Research Plan in Shaanxi Province of China (Grant No. 2020JM-120).

APPENDIX

1. Spin density distribution on carbon crosses

With EOM-CCSD calculations, we obtain 12 singlet states and 20 triplet states for Ni_2C_{24} and 12 singlet states and 15 triplet states for Ni_2C_{44}. Taking the single states obtained by CCSD calculations into account, there are 73 many-body

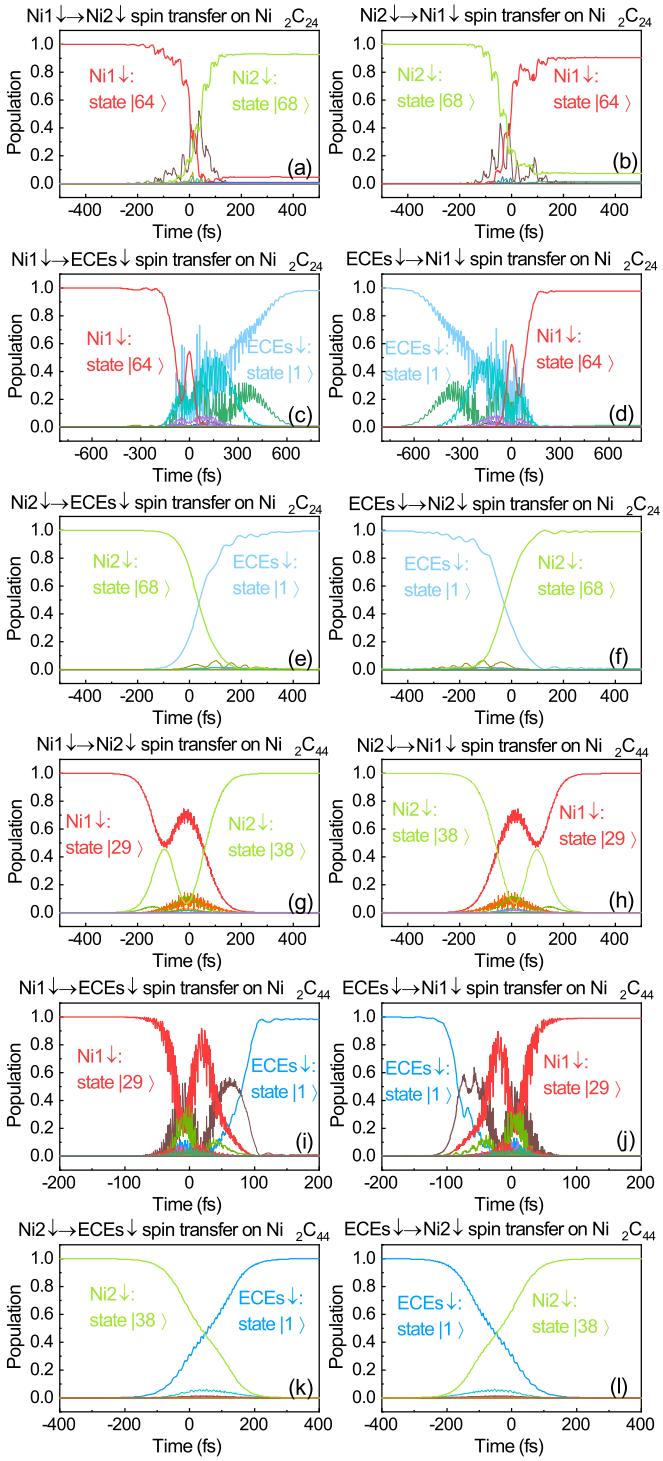

FIG. 8. The Ni2 → Ni1, Ni1 → ECEs, ECEs → Ni1, Ni2 → ECEs, and ECEs → Ni2 spin-transfer processes on Ni_2C_{24} and Ni_2C_{44}. The red lines denote the states with spin localized on Ni1 and the green lines denote the states with spin localized on Ni2. The states with spin localized on ECEs are denoted by the blue lines. The lines in other colors denote the intermediate states.

states found for Ni_2C_{24} ($12 \times 1 + 20 \times 3 + 1 = 73$, shown in Table III) and 58 many-body states found for Ni_2C_{44} ($12 \times 1 + 15 \times 3 + 1 = 58$, shown in Table IV).

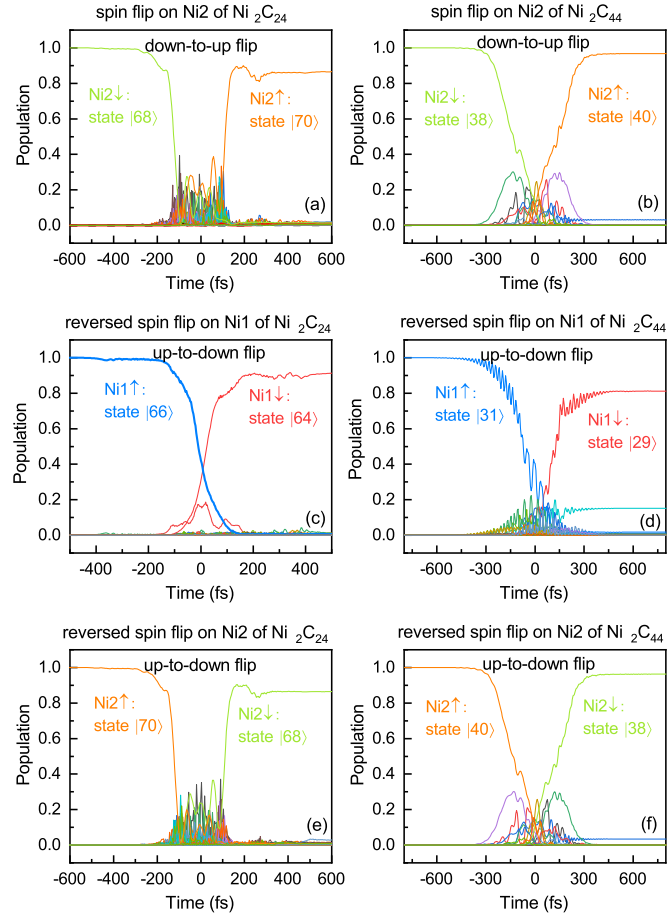

FIG. 9. The local spin-flip processes on the two Ni atoms of Ni_2C_{24} and Ni_2C_{44}. Panels (a) and (b) depict the down-to-up spin flip on the Ni2 atoms of Ni_2C_{24} and Ni_2C_{44}, respectively. Panels (c) and (d) depict the reversed spin flip from up to down on the Ni1 atoms of Ni_2C_{24} and Ni_2C_{44}. Panels (e) and (f) depict the reversed spin flip from up to down on the Ni2 atoms of Ni_2C_{24} and Ni_2C_{44}. The red and blue lines denote the spin-down and spin-up states with spin localized on Ni1, respectively. The green and orange lines denote the spin-down and spin-up states with spin localized on Ni2, respectively. The lines in other colors denote the intermediate states.

2. Spin-transfer scenarios on carbon crosses

Figures 8 depict all the available spin-down-transfer scenarios among the three spin centers on Ni_2C_{24} and Ni_2C_{44}, including the reversed spin-down-transfer scenarios. Due to the same interaction scenarios between the laser pulses and the many-body states, the reversed spin-transfer processes are nearly the reflections of the original processes.

3. Spin-flip scenarios on carbon crosses

Figure 9 illustrates the spin-flip process on the Ni2 atoms of the two carbon cross structures. For the smaller structure Ni_2C_{24}, the states $|68\rangle$ (spin down) and $|70\rangle$ (spin up), which stem from the same triplet state, are taken as the initial and target states, respectively. As for the larger structure Ni_2C_{44}, the initial and target states are the states $|38\rangle$ (spin down) and $|40\rangle$ (spin up), respectively. The reversed spin-flip processes from spin up to spin down are also illustrated

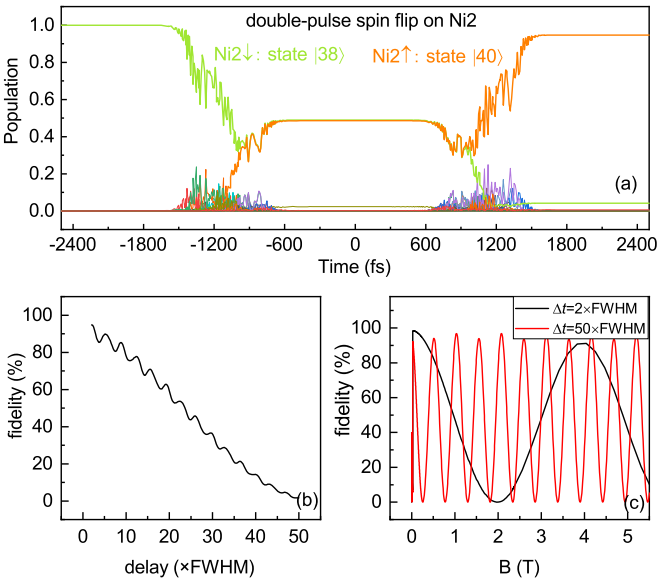

FIG. 10. The double-pulse-induced spin-flip processes on Ni2 of Ni_2C_{44}. Panel (a) depicts the time evolution of the population of the initial, target, and intermediate states with a delay between the two pulses of two times the FWHM. Panel (b) depicts the fidelity of the double-pulse spin flip on Ni1 with a different delay between two laser pulses. Panel (c) depicts the corresponding fidelity of the spin-flip scenarios under the different magnetic field with a delay of two times (black line) and 50 times the FWHM (red line), respectively.

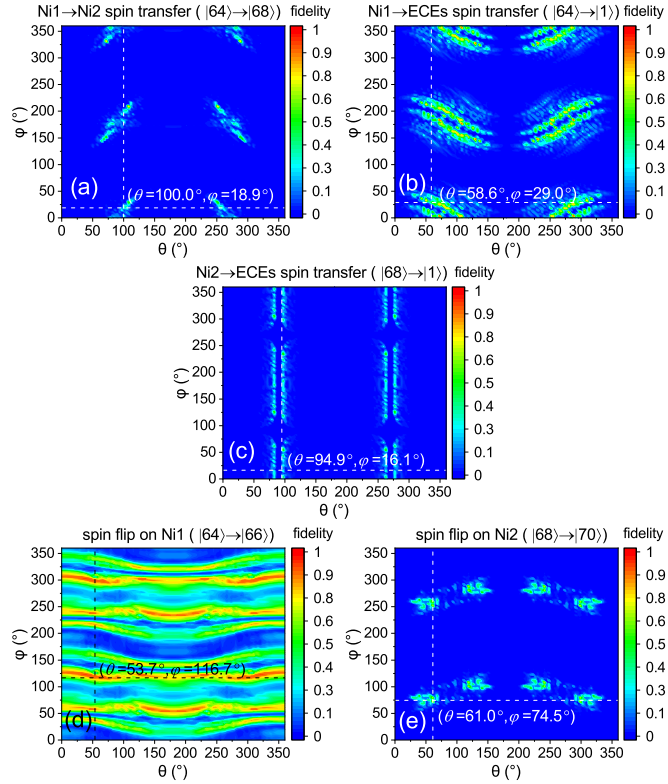

FIG. 11. The fidelity of Ni1 → Ni2 spin transfer (a), Ni1 → ECEs spin transfer (b), Ni2 → ECEs spin transfer (c), spin flip on Ni1 (d), and spin flip on Ni2 (e) of Ni_2C_{24} with different laser directions. The crossover point of the two dashed lines in each panel denotes the resonant direction of the laser pulse optimized by our genetic algorithm program.

in Fig. 9. Since the electronic configurations of the initial and target states are quite similar, the reversed spin-flip processes are nearly equivalent to the original processes simply by exchanging the population of the spin-up and spin-down states.

4. Double-pulse-induced spin dynamics

States $|38\rangle$ and $|40\rangle$ are chosen as the initial and target states for the double-pulse spin flip on Ni2, respectively. The parameters of the optimized laser pulse are $\theta = 169.7°$, $\phi = 7.6°$, $\gamma = 88.6°$, amplitude $= 4.783 \times 10^9$ V/m, FWHM $=$ 310 fs, $E_{\text{laser}} = 3.724$ eV, chirp $= 1.59\%$, and the delay is set as double FWHM. The fidelity reaches a high value of 94.7% [Fig. 10(a)]. By increasing the time delay, this double-pulse spin-flip process can also be blocked [Fig. 10(b)]. If the gradient of the magnetic field strength is 10 T/μm [76–81], the shortest distance between two identical Ni2 atoms is around 93.7 nm for individually addressing each magnetic center, and it can be shortened to 9.7 nm by increasing the delay to 50 times FWHM [Fig. 10(c)].

5. Effect of the direction of the laser pulse

Similar to the scenarios of Ni_2C_{44}, a small deviation of laser pulse from the resonant direction can result in a substantial drop of fidelity of the spin-dynamic process (Fig. 11). Since there are more intermediate states involved in the spin-dynamic processes on Ni_2C_{24}, which indicates that the interaction between laser and many-body states is more complicated, such a phenomenon is even more apparent.

[1] E. Beaurepaire, J.-C. Merle, A. Daunois, and J.-Y. Bigot, Ultrafast Spin Dynamics in Ferromagnetic Nickel, Phys. Rev. Lett. **76**, 4250 (1996).

[2] G. P. Zhang and W. Hübner, Laser-Induced Ultrafast Demagnetization in Ferromagnetic Metals, Phys. Rev. Lett. **85**, 3025 (2000).

[3] C. D. Stanciu, A. Tsukamoto, A. V. Kimel, F. Hansteen, A. Kirilyuk, A. Itoh, and T. Rasing, Subpicosecond Magnetization Reversal across Ferrimagnetic Compensation Points, Phys. Rev. Lett. **99**, 217204 (2007).

[4] U. Atxitia, O. Chubykalo-Fesenko, R. W. Chantrell, U. Nowak, and A. Rebei, Ultrafast Spin Dynamics: The Effect of Colored Noise, Phys. Rev. Lett. **102**, 057203 (2009).

[5] C. Boeglin, E. Beaurepaire, V. Halté, V. López-Flores, C. Stamm, N. Pontius, H. A. Dürr, and J.-Y. Bigot, Distinguishing the ultrafast dynamics of spin and orbital moments in solids, Nature (London) **465**, 458 (2010).

[6] U. Atxitia and O. Chubykalo-Fesenko, Ultrafast magnetization dynamics rates within the Landau-Lifshitz-Bloch model, Phys. Rev. B **84**, 144414 (2011).

[7] T. Roth, A. J. Schellekens, S. Alebrand, O. Schmitt, D. Steil, B. Koopmans, M. Cinchetti, and M. Aeschlimann, Temperature Dependence of Laser-Induced Demagnetization in Ni: A Key for Identifying the Underlying Mechanism, Phys. Rev. X **2**, 021006 (2012).

[8] B. Pfau, S. Schaffert, L. Müller, C. Gutt, A. Al-Shemmary, F. Büttner, R. Delaunay, S. Düsterer, S. Flewett, R. Frümter, J. Geilhufe, E. Guehrs, C. Günther, R. Hawaldar, M. Hille, N. Jaouen, A. Kobs, K. Li, J. Mohanty, H. Redlin *et al.*, Ultrafast optical demagnetization manipulates nanoscale spin structure in domain walls, Nat. Commun. **3**, 1100 (2012).

[9] S. Mangin, M. Gottwald, C.-H. Lambert, D. Steil, V. Uhlíř, L. Pang, M. Hehn, S. Alebrand, M. Cinchetti, G. Malinowski, Y. Fainman, M. Aeschlimann, and E. E. Fullerton, Engineered materials for all-optical helicity-dependent magnetic switching, Nat. Mater. **13**, 286 (2014).

[10] C.-H. Lambert, S. Mangin, B. S. D. C. S. Varaprasad, Y. K. Takahashi, M. Hehn, M. Cinchetti, G. Malinowski, K. Hono, Y. Fainman, M. Aeschlimann, and E. E. Fullerton, All-optical control of ferromagnetic thin films and nanostructures, Science **345**, 1337 (2014).

[11] H. H. Guo, J. L. Liao, B. Ma, Z. Z. Zhang, Q. Y. Jin, H. Wang, and J. P. Wang, Microstructure and magnetization reversal of $L1_0$-FePt/$[Co/Pt]_N$ exchange coupled composite films, Appl. Phys. Lett. **100**, 142406 (2012).

[12] S. Saha, S. Barman, Y. Otani, and A. Barman, All-optical investigation of tunable picosecond magnetization dynamics in ferromagnetic nanostripes with a width down to 50 nm, Nanoscale **7**, 18312 (2015).

[13] O. Morandi and P.-A. Hervieux, Ultrafast dynamics in ferrimagnetic materials with a quantum Monte Carlo atomistic model, Phys. Rev. B **96**, 024441 (2017).

[14] Wikipedia contributors: "MOSFET," https://en.wikipedia.org/wiki/MOSFET.

[15] S. Joshi, J. T. Liao, Y. Fan, S. Hyvonen, M. Nagarajan, J. Rizk, H. Lee, and I. Young, A 12-Gb/s transceiver in 32-nm bulk CMOS, in *Proceedings of the 2009 Symposium on VLSI Circuits* (IEEE, Kyoto, Japan, 2009), pp. 52–53.

[16] S. Narasimha, B. Jagannathan, A. Ogino, D. Jaeger, B. Greene, C. Sheraw, K. Zhao, B. Haran, U. Kwon, A. K. M. Mahalingam, B. Kannan, B. Morganfeld, J. Dechene, C. Radens, A. Tessier, *et al.*, A 7nm CMOS technology platform for mobile and high performance compute application, in *Proceedings of the 2017 IEEE International Electron Devices Meeting (IEDM)* (IEEE, San Francisco, CA, USA, 2017), pp. 29.5.1–29.5.4.

[17] I. Žutić, J. Fabian, and S. Das Sarma, Spintronics: Fundamentals and applications, Rev. Mod. Phys. **76**, 323 (2004).

[18] F. Pulizzi, Spintronics, Nat. Mater. **11**, 367 (2012).

[19] B. Dieny, I. L. Prejbeanu, K. Garello, P. Gambardella, P. Freitas, R. Lehndorff, W. Raberg, U. Ebels, S. O. Demokritov, J. Akerman, A. Deac, P. Pirro, C. Adelmann, A. Anane, A. V. Chumak, A. Hirohata, S. Mangin, S. O. Valenzuela, M. C. Onbaşl, M. d'Aquino *et al.*, Opportunities and challenges for spintronics in the microelectronics industry, Nat. Electron. **3**, 446 (2020).

[20] A. Hirohata, K. Yamada, Y. Nakatani, I.-L. Prejbeanu, B. Diény, P. Pirro, and B. Hillebrands, Review on spintronics: Principles and device applications, J. Magn. Magn. Mater. **509**, 166711 (2020).

[21] V. A. Dediu, L. E. Hueso, I. Bergenti, and C. Taliani, Spin routes in organic semiconductors, Nat. Mater. **8**, 707 (2009).

[22] A. Sukhov and J. Berakdar, Local Control of Ultrafast Dynamics of Magnetic Nanoparticles, Phys. Rev. Lett. **102**, 057204 (2009).

[23] T. Brächer and P. Pirro, An analog magnon adder for all-magnonic neurons, J. Appl. Phys. **124**, 152119 (2018).

[24] V. Dediu, M. Murgia, F. Matacotta, C. Taliani, and S. Barbanera, Room temperature spin polarized injection in organic semiconductor, Solid State Commun. **122**, 181 (2002).

[25] Z. H. Xiong, D. Wu, Z. V. Vardeny, and J. Shi, Giant magnetoresistance in organic spin-valves, Nature (London) **427**, 821 (2004).

[26] B. Koopmans, J. J. M. Ruigrok, F. Dalla Longa, and W. J. M. de Jonge, Unifying Ultrafast Magnetization Dynamics, Phys. Rev. Lett. **95**, 267207 (2005).

[27] J. K. Dewhurst, P. Elliott, S. Shallcross, E. K. U. Gross, and S. Sharma, Laser-induced intersite spin transfer, Nano Lett. **18**, 1842 (2018).

[28] D. Steil, J. Walowski, F. Gerhard, T. Kiessling, D. Ebke, A. Thomas, T. Kubota, M. Oogane, Y. Ando, J. Otto, A. Mann, M. Hofherr, P. Elliott, J. K. Dewhurst, G. Reiss, L. Molenkamp, M. Aeschlimann, M. Cinchetti, M. Münzenberg, S. Sharma *et al.*, Efficiency of ultrafast optically induced spin transfer in heusler compounds, Phys. Rev. Research **2**, 023199 (2020).

[29] M. Battiato, K. Carva, and P. M. Oppeneer, Superdiffusive Spin Transport as a Mechanism of Ultrafast Demagnetization, Phys. Rev. Lett. **105**, 027203 (2010).

[30] J.-Y. Bigot, M. Vomir, and E. Beaurepaire, Coherent ultrafast magnetism induced by femtosecond laser pulses, Nat. Phys. **5**, 515 (2009).

[31] N. Kazantseva, U. Nowak, R. W. Chantrell, J. Hohlfeld, and A. Rebei, Slow recovery of the magnetisation after a sub-picosecond heat pulse, Europhys. Lett. **81**, 27004 (2008).

[32] U. Atxitia, O. Chubykalo-Fesenko, N. Kazantseva, D. Hinzke, U. Nowak, and R. W. Chantrell, Micromagnetic modeling of laser-induced magnetization dynamics using the Landau-Lifshitz-Bloch equation, Appl. Phys. Lett. **91**, 232507 (2007).

[33] U. Atxitia, O. Chubykalo-Fesenko, J. Walowski, A. Mann, and M. Münzenberg, Evidence for thermal mechanisms in laser-induced femtosecond spin dynamics, Phys. Rev. B **81**, 174401 (2010).

[34] E. Moreno-Pineda, C. Godfrin, F. Balestro, W. Wernsdorfer, and M. Ruben, Molecular spin qudits for quantum algorithms, Chem. Soc. Rev. **47**, 501 (2018).

[35] M. Atzori and R. Sessoli, The second quantum revolution: Role and challenges of molecular chemistry, J. Am. Chem. Soc. **141**, 11339 (2019).

[36] A. Gaita-Ariño, F. Luis, S. Hill, and E. Coronado, Molecular spins for quantum computation, Nat. Chem. **11**, 301 (2019).

[37] A. Chiesa, E. Macaluso, F. Petiziol, S. Wimberger, P. Santini, and S. Carretta, Molecular nanomagnets as qubits with embedded quantum-error correction, J. Phys. Chem. Lett. **11**, 8610 (2020).

[38] S. Carretta, D. Zueco, A. Chiesa, A. Gómez-León, and F. Luis, A perspective on scaling up quantum computation with molecular spins, Appl. Phys. Lett. **118**, 240501 (2021).

[39] G. D. Mahan, Spin Shift Register from a One-Dimensional Atomic Chain, Phys. Rev. Lett. **102**, 016801 (2009).

[40] F. Luis, A. Repollés, M. J. Martínez-Pérez, D. Aguilà, O. Roubeau, D. Zueco, P. J. Alonso, M. Evangelisti, A. Camón, J. Sesé, L. A. Barrios, and G. Aromí, Molecular Prototypes for Spin-Based CNOT and SWAP Quantum Gates, Phys. Rev. Lett. **107**, 117203 (2011).

[41] M. D. Jenkins, Y. Duan, B. Diosdado, J. J. García-Ripoll, A. Gaita-Ariño, C. Giménez-Saiz, P. J. Alonso, E. Coronado, and F. Luis, Coherent manipulation of three-qubit states in a molecular single-ion magnet, Phys. Rev. B **95**, 064423 (2017).

[42] C. Godfrin, A. Ferhat, R. Ballou, S. Klyatskaya, M. Ruben, W. Wernsdorfer, and F. Balestro, Operating Quantum States in Single Magnetic Molecules: Implementation of Grover's Quantum Algorithm, Phys. Rev. Lett. **119**, 187702 (2017).

[43] E. Macaluso, M. Rubín, D. Aguilà, A. Chiesa, L. A. Barrios, J. I. Martínez, P. J. Alonso, O. Roubeau, F. Luis, G. Aromí, and S. Carretta, A heterometallic [LnLn'Ln] lanthanide complex as a qubit with embedded quantum error correction, Chem. Sci. **11**, 10337 (2020).

[44] J. Liu, J. Mrozek, A. Ullah, Y. Duan, J. J. Baldoví, E. Coronado, A. Gaita-Ariño, and A. Ardavan, Quantum coherent spin-electric control in a molecular nanomagnet at clock transitions, Nat. Phys. **17**, 1205 (2021).

[45] C. Li, S. Zhang, W. Jin, G. Lefkidis, and W. Hübner, Controllable spin-dynamics cycles and ERASE functionality on quasilinear molecular ions, Phys. Rev. B **89**, 184404 (2014).

[46] G. Lefkidis, W. Jin, J. Liu, D. Dutta, and W. Hübner, Topological spin-charge gearbox on a real molecular magnet, J. Phys. Chem. Lett. **11**, 2592 (2020).

[47] S. Sold, B. C. Mummaneni, N. C. Michenfelder, Y. Peng, A. K. Powell, A.-N. Unterreiner, G. Lefkidis, and W. Hubner, Experimental and theoretical study of the ultrafast dynamics of a Ni2Dy2-compound in DMF after UV/Vis photoexcitation, ChemistryOpen **10**, 1 (2021).

[48] B. C. Mummaneni, J. Liu, G. Lefkidis, and W. Hübner, Laser-controlled implementation of controlled-NOT, Hadamard, SWAP, and Pauli gates as well as generation of Bell states in a 3d-4f molecular magnet, J. Phys. Chem. Lett. **13**, 2479 (2022).

[49] L. Jia, J. Wu, Y. Zhang, Y. Qu, B. Jia, Z. Chen, and D. J. Moss, Fabrication technologies for the on-chip integration of 2D materials, Small Methods **6**, 2101435 (2022).

[50] J.-H. Kim, S. Aghaeimeibodi, J. Carolan, D. Englund, and E. Waks, Hybrid integration methods for on-chip quantum photonics, Optica **7**, 291 (2020).

[51] D. Sarkar, X. Xie, J. Kang, H. Zhang, W. Liu, J. Navarrete, M. Moskovits, and K. Banerjee, Functionalization of transition metal dichalcogenides with metallic nanoparticles: Implications for doping and gas-sensing, Nano Lett. **15**, 2852 (2015).

[52] L. Cai, C. J. McClellan, A. L. Koh, H. Li, E. Yalon, E. Pop, and X. Zheng, Rapid flame synthesis of atomically thin MoO_3 down to monolayer thickness for effective hole doping of WSe_2, Nano Lett. **17**, 3854 (2017).

[53] T. Kim, P. Bhargava, C. V. Poulton, J. Notaros, A. Yaacobi, E. Timurdogan, C. Baiocco, N. Fahrenkopf, S. Kruger, T. Ngai, Y. Timalsina, M. R. Watts, and V. Stojanović, A single-chip optical phased array in a wafer-scale silicon photonics/CMOS 3D-integration platform, IEEE J. Solid-State Circ. **54**, 3061 (2019).

[54] J. Sun, E. Shah Hosseini, A. Yaacobi, D. B. Cole, G. Leake, D. Coolbaugh, and M. R. Watts, Two-dimensional apodized silicon photonic phased arrays, Opt. Lett. **39**, 367 (2014).

[55] M. J. Heck, Highly integrated optical phased arrays: photonic integrated circuits for optical beam shaping and beam steering, Nanophotonics **6**, 93 (2017).

[56] I. Aharonovich, D. Englund, and M. Toth, Solid-state single-photon emitters, Nat. Photon. **10**, 631 (2016).

[57] J. Liu, C. Li, W. Jin, G. Lefkidis, and W. Hübner, Long-Distance Ultrafast Spin Transfer over a Zigzag Carbon Chain Structure, Phys. Rev. Lett. **126**, 037402 (2021).

[58] H. Du, J. Liu, N. Zhang, J. Chang, W. Jin, C. Li, G. Lefkidis, and W. Hübner, Theoretical study of laser-induced ultrafast spin dynamics in small iron-benzene clusters and of related laser and magnetic-field effects, Phys. Rev. B **99**, 134430 (2019).

[59] W. Han, R. K. Kawakami, M. Gmitra, and J. Fabian, Graphene spintronics, Nat. Nanotechnol. **9**, 794 (2014).

[60] M. Zeng, L. Shen, M. Zhou, C. Zhang, and Y. Feng, Graphene-based bipolar spin diode and spin transistor: Rectification and amplification of spin-polarized current, Phys. Rev. B **83**, 115427 (2011).

[61] Y. Zhang, J. Liu, C. Li, W. Jin, G. Lefkidis, and W. Hübner, Strain-promoted reversible spin transfer in rhombic graphene nanoflakes, Appl. Surf. Sci. **558**, 149770 (2021).

[62] Y. Zhang, J. Liu, W. Jin, G. Lefkidis, W. Hübner, and C. Li, Two-qubit logic gates based on the ultrafast spin transfer in π-conjugated graphene nanoflakes, Carbon **193**, 195 (2022).

[63] C. Li, S. Zhang, W. Jin, G. Lefkidis, and W. Hübner, Λ-process-based spin manipulation in magnetic endohedral fullerenes, IEEE Trans. Magn. **49**, 3195 (2013).

[64] C. Li, J. Liu, S. Zhang, G. Lefkidis, and W. Hübner, Strain assisted ultrafast spin switching on $Co_2@C_{60}$ endohedral fullerenes, Carbon **87**, 153 (2015).

[65] C. Li, J. Liu, S. Zhang, G. Lefkidis, and W. Hübner, Strain effect on the ultrafast spin switching of cobalt-doped carbon fullerenes, IEEE Trans. Magn. **51**, 1 (2015).

[66] J. Liu, Y. Zhang, C. Li, W. Jin, G. Lefkidis, and W. Hübner, Magneto-straintronics on a Co-coordinating metalloboron-fullerene, Phys. Rev. B **102**, 024416 (2020).

[67] G. Lefkidis and W. Hübner, First-principles study of ultrafast magneto-optical switching in NiO, Phys. Rev. B **76**, 014418 (2007).

[68] G. Lefkidis, G. P. Zhang, and W. Hübner, Angular Momentum Conservation for Coherently Manipulated Spin Polarization in Photoexcited NiO: An *Ab Initio* Calculation, Phys. Rev. Lett. **103**, 217401 (2009).

[69] W. Hübner, S. Kersten, and G. Lefkidis, Optical spin manipulation for minimal magnetic logic operations in metallic three-center magnetic clusters, Phys. Rev. B **79**, 184431 (2009).

[70] R. R. Cash and A. H. Karp, A variable order Runge-Kutta method for initial value problems with rapidly varying right-hand sides, ACM Trans. Math. Softw. **16**, 201 (1990).

[71] T. Hartenstein, C. Li, G. Lefkidis, and W. Hübner, Local light-induced spin manipulation in two magnetic centre metallic chains, J. Phys. D **41**, 164006 (2008).

[72] C. Li, W. Jin, H. Xiang, G. Lefkidis, and W. Hübner, Theory of laser-induced ultrafast magneto-optic spin flip and transfer in charged two-magnetic-center molecular ions: Role of bridging atoms, Phys. Rev. B **84**, 054415 (2011).

[73] S. L. Bayliss, D. W. Laorenza, P. J. Mintun, B. D. Kovos, D. E. Freedman, and D. D. Awschalom, Optically addressable

molecular spins for quantum information processing, Science **370**, 1309 (2020).

[74] V. Westphal and S. W. Hell, Nanoscale Resolution in the Focal Plane of an Optical Microscope, Phys. Rev. Lett. **94**, 143903 (2005).

[75] R. Schmidt, C. A. Wurm, S. Jakobs, J. Engelhardt, A. Egner, and S. W. Hell, Spherical nanosized focal spot unravels the interior of cells, Nat. Methods **5**, 539 (2008).

[76] J. Wróbel, T. Dietl, A. Łusakowski, G. Grabecki, K. Fronc, R. Hey, K. H. Ploog, and H. Shtrikman, Spin Filtering in a Hybrid Ferromagnetic-Semiconductor Microstructure, Phys. Rev. Lett. **93**, 246601 (2004).

[77] M. Pioro-Ladrière, T. Obata, Y. Tokura, Y.-S. Shin, T. Kubo, K. Yoshida, T. Taniyama, and S. Tarucha, Electrically driven single-electron spin resonance in a slanting Zeeman field, Nat. Phys. **4**, 776 (2008).

[78] M. Kustov, P. Laczkowski, D. Hykel, K. Hasselbach, F. Dumas-Bouchiat, D. O'Brien, P. Kauffmann, R. Grechishkin, D. Givord, G. Reyne, O. Cugat, and N. M. Dempsey, Magnetic characterization of micropatterned Nd-Fe-B hard magnetic films using scanning hall probe microscopy, J. Appl. Phys. **108**, 063914 (2010).

[79] H. J. Mamin, C. T. Rettner, M. H. Sherwood, L. Gao, and D. Rugar, High field-gradient dysprosium tips for magnetic resonance force microscopy, Appl. Phys. Lett. **100**, 013102 (2012).

[80] B. Schüler, M. Cerchez, H. Xu, J. Schluck, T. Heinzel, D. Reuter, and A. D. Wieck, Observation of quantum states without a semiclassical equivalence bound by a magnetic field gradient, Phys. Rev. B **90**, 201111(R) (2014).

[81] N. M. Dempsey, D. L. Roy, H. Marelli-Mathevon, G. Shaw, A. Dias, R. B. G. Kramer, L. V. Cuong, M. Kustov, L. F. Zanini, C. Villard, K. Hasselbach, C. Tomba, and F. Dumas-Bouchiat, Micro-magnetic imprinting of high field gradient magnetic flux sources, Appl. Phys. Lett. **104**, 262401 (2014).

[82] D. Chaudhuri, W. Jin, G. Lefkidis, and W. Hübner, Ab initio theory for femtosecond spin dynamics, angle-resolved fidelity analysis, and the magneto-optical kerr effect in the $Ni_3(CH_3$ OH) and $Co_3^+(CH_3$ OH) clusters, J. Chem. Phys. **143**, 174303 (2015).